博士論文

Anode properties of magnesium hydride with all solid state lithium ion batteries

（全固体リチウムイオン電池を用いた水素化マグネシウムの負極特性）

池田　卓

広島大学大学院先端物質科学研究科

2014 年 3 月

目次

主論文

Abstract

Magnesium hydride (MgH_2) has a potential as an anode material for LIBs and it is one of candidates to satisfy the future market demands. Actually, MgH_2 reacts with lithium (Li) and is transformed into Mg and lithium hydride (LiH), showing large reversible capacity of 1480 mAh g^{-1} with an average voltage of 0.5V versus Li^+/Li ($MgH_2 + 2Li^+ + 2e^- \leftrightarrow Mg + 2LiH$). In this thesis, anode properties of MgH_2 with all solid state lithium ion batteries cell are investigated. In particular, the relationship between the hydrogen desorption properties and electrochemical properties of MgH_2 is focused on to improve battery properties of LIBs. It has been well known that metal oxides improve the hydrogen ab/desorbing properties of MgH_2. The purpose of this thesis is to clarify the role of additive metal oxide to MgH_2 as anode for all solid state LIBs.

The results obtained in this thesis summarized as follows;

1. Pristine MgH_2 reacts with Li ions electrochemically, producing Mg and LiH even if the experiments were performed with all solid state LIBs. Coulombic efficiency of the first cycle is 26%, indicating that 74% of the entering Li ions remained in the electrode.In the case of Nb_2O_5 doped MgH_2, coulombic efficiency of the first cycle was improved from 26% (pristine MgH_2) to 37% ($99MgH_2$-$1Nb_2O_5$) by adding Nb_2O_5. Moreover, coulombic efficiency was increased from 37% to 56% with increasing Nb_2O_5 contents (Nb_2O_5 contents: 0 mol% to 5 mol%). Effects of the Nb_2O_5 additive on anode properties at high current or at low temperature were clearer than that at low current density or at high temperature. The hydrogen desorption temperature decreases with

increasing Nb_2O_5 contents, and coulombic efficiency was increased with increasing Nb_2O_5 contents. Namely, coulombic efficiency was increased with decreasing hydrogen desorption temperature.

2. In the case of Al_2O_3 doped MgH_2, first coulombic efficiency was improved from 26% (pristine MgH_2) to 39% ($99MgH_2$-$1Al_2O_3$) by adding Al_2O_3. Moreover, coulombic efficiency was increased from 26% to 52% with increasing Al_2O_3 contents (Al_2O_3 contents: 0 mol% to 25 mol%). The hydrogen desorption temperature did not decrease with increasing Al_2O_3 contents. On the other hand, coulombic efficiency was increased with increasing Al_2O_3 contents. Namely, coulombic efficiency was improved by Al_2O_3, but hydrogen desorption temperature did not depend on Al_2O_3 contents. In order to obtain the local structural information and to clarify that why columbic efficiency was increased by adding Al_2O_3, ^{27}Al-MAS-NMR of Al_2O_3 doped MgH_2 was carried out. It is known that Al atom in γ-Al_2O_3 occupied octahedral coordination (AlO_6) and tetrahedral coordination (AlO_4). In the case of $75MgH_2$-$25Al_2O_3$, the distribution of AlO_6 was increased and the distribution of AlO_4 was decreased after Li insertion reaction. In addition, peak position of octahedral coordination shifts slightly to high magnetic field region and pentahedral coordination (AlO_5) is observed at around 33 ppm. This could act as a binding site for LiH. As a result, the path of hydrogen diffusion between Mg phase and LiH phase is remained, leading to the increasing of coulombic efficiency.

Acknowledgements

I would like to express my gratitude to my supervisor Prof. Dr. Yoshitsugu Kojima for his insightful comments and suggestions throughout the course of this work.

I would like to express my special thanks to Associate Prof. Dr. Takayuki Ichikawa for his constructive comments and warm encouragement in my doctoral course life.

I would like to express my special thanks to Lecturer. Dr. Hiroki Miyaoka for his valuable suggestions and discussions.

I am deeply grateful to Prof. Dr. Masafumi Sera, Prof. Dr. Toshiro Takabatake, and Assistant Prof. Hiroshi Tanida for their helpful suggestion and discussion.

I would like to express my special thanks to the colleagues of Prof. Kojima's Laboratory, Dr. Keiji Shimoda, Dr. Aki Yamane, Dr. Ankur Jain, Dr. Hitoshi Inokawa, Mr. Toru Kimura, Mr. Koji kawahito, Mr. Kiyotaka Gosyome, Mr. Kei Kubota, Mr. Kazuhiro Hirabayashi, Mr. Naoya Nakamura, Mr. Taihei Aoki, Ms. Erika Kawasako, Mr. Koichi Tanimoto, Mr. Shotaro Yamaguchi, Mr. Takahiro Okuda, and Mr. TakahiroYamada.

Finally, I would like to express my special thanks to Ms. Misao Mukoda and Ms. Saori Inagaki for their support in my doctoral course life.

Contents

1 Introduction

1-1 Lithium ion batteries

Rechargeable battery technology is indispensable for our current society. For example, automobiles equipped originally lead-acid batteries for ignition, lighting and other electrical system as power source. Nickel-cadmium (Ni-Cd) batteries have been well known as the most suitable battery of power tool. Recently, nickel-metal hydride (Ni-MH) batteries and lithium ion batteries (LIBs) are utilized instead of Ni-Cd batteries. Fig. 1-1 shows volumetric and gravimetric energy density of different batteries.

LIBs have high density energy as shown in Fig. 1-1, because lithium has essentially the most electronegative potential (-3.04V) as a standard value and it is the lightest metal (0.534g cm^{-3}, 6.94g mol^{-1}). Therefore, LIBs have been utilized for many portable devices, such as mobile phones, lap-top computers, and power tools. Thus, LIBs are regarded as fatal devices in our society. In the future, LIBs will be key devices for energy storage to achieve a highly energy-efficient society. In particular, for the utilization of renewable energy sources such as solar, tidal, and wind power, highly functional secondary batteries should be developed to supply electricity on-demand originating from renewable energy sources, because of the specific properties with fluctuation and maldistribution. LIBs could be vital devices as candidates for functional batteries to utilize renewable energy efficiently in the future.

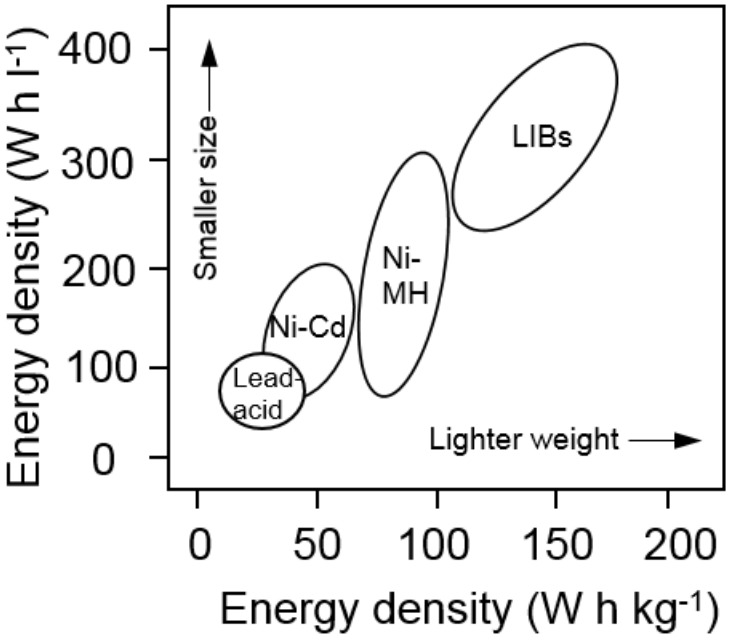

Figure 1-1 Volumetric and gravimetric energy density of different battery technologies [1-1]

The LIB is mainly composed of anode, cathode, and electrolyte. The electrolyte separates anode and cathode physically to prevent an electrical short. The anode absorbs (desorbs) lithium ions on the charge (discharge) reaction. On the other hand, the cathode desorbs (absorbs) lithium ions on the charge (discharge) reaction. Namely, on the discharge reaction, lithium ions in the anode move into cathode through the electrolyte. At the same time electrons are generated in anode as follows, and then move into cathode through external circuit to work.

$$Li \rightarrow Li^{+} + e^{-}$$

Thus, two electrodes must have electronic and lithium ion conductive functions and electrolyte must be lithium ion conductor and electronic insulator. Many types of

cathode materials, anode materials, and electrolytes have already been reported so far as bellow.

1-1-1 Cathode materials

Cathode materials are required to have electropositive standard electrode potential. In addition, they should possess electric conductivity and lithium ionic conductivity to utilize them as a cathode electrode. Representative fundamental cathode materials are $LiCoO_2$, $LiMn_2O_4$, $LiFePO_4$, and so on.

1-1-2 Anode materials

Anode materials are required to have electronegative standard electrode potential, so lithium metal is the ultimate anode material. However, the lithium metal with a dendrite shape grows on the surface of lithium electrode during charge reaction when lithium metal is used as anode materials. Because the dendrite causes internal short, it is impossible to utilize lithium metal as anode material on the view point of safety.

Various kinds of materials have been used for Li insertion-extraction reactions as anode materials in the most commercial LIBs. For example, carbon based materials or $Li_4Ti_5O_{12}$ have been attempted so far. Furthermore, alloy-dealloy reaction materials and conversion reaction materials are regarded as promising candidate materials for anode. However, they have not been used practically so far.

1-1-2-1 Insertion-extraction reaction materials

The anode made of easily-graphitizable carbon (soft carbon) was utilized as the first generation commercial LIB by Sony Corp., which showed 250 mAh g^{-1} in the capacity.

Soft carbon has randomly-collapsed structure compared with crystalline graphite and it easily changes to well-ordered graphite crystal structure by heat treatment. Soft carbon which has high capacity of approximately 400 mAh g^{-1} to 900 mAh g^{-1} showed low first columbic efficiency and poor cycle properties. Therefore, it has not been used practically.

The hardly graphitizable carbon (hard carbon) is one of carbon based anode materials. Its graphitization does not proceed by heat treatment even at 3000 °C. Hard carbon has randomly-orientated crystallite of graphite. In addition, the inter layer distance of hard carbon is more than 0.38 nm. Therefore, hard carbon does not expand through lithium intercalation. This leads to good cycle and rate properties. In 1992, Sony Corp. developed the LIB whose anode material is made of hard carbon for the video camera.

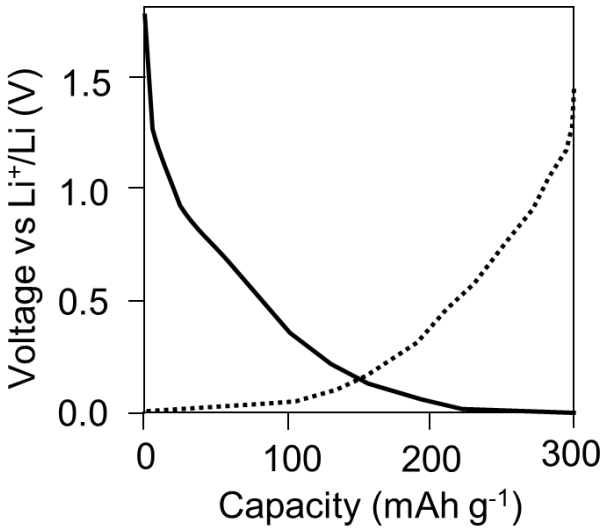

Figure 1-2 Li insertion (solid line) and extraction (dotted line) curves of the Carbotron P(J) [1-2]

Fig 1-2 shows Li insertion (charge) and extraction (discharge) curves of the Cabotron P(J) by KUREHA. The charge and discharge curves show gentle slope between 0 and 1

V, meaning that it is easy to measure the remaining capacity of a LIB cell by measuring cell voltage. Therefore, hard carbon is utilized partly for LIBs of the hybrid electric vehicle recently.

Graphite has the electronegative standard electrode potential of 0.07 V to 0.23 V versus Li^+/Li potential, and its theoretical capacity is 372 mAh g^{-1} as shown in Fig1-3. In addition, graphite does not show structural change during lithium intercalation (charge) or deintercalation (discharge) reaction except only slight volume expansion (less than 10%) along to only c-axis, so graphite shows good cycle properties. Thus, graphite has excellent anode properties and cost merit due to abundant resources. Therefore, graphite is utilized most commonly as anode material for current commercial LIBs in all over the world.

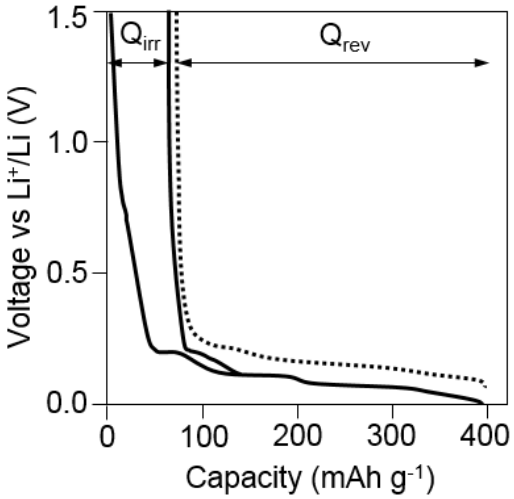

Figure 1-3 Li intercalation (solid line) and Li deintercalation (dotted line) curves of graphite. Q_{irr} and Q_{rev} represent irreversible capacity and reversible capacity [1-3]

Lithium ions intercalate into interlayer of graphite up to 1 lithium ion per 6 carbon atoms as follows,

$$C_6 + Li^+ + e^- \leftrightarrow C_6Li.$$

$L_4Ti_{15}O_{12}$ (LTO) shows slight volume expansion and shrinkage during lithium insertion and extraction reaction and it is called “zero-strain insertion material” [1-4-5]. This indicates that LTO has superior cycle properties. Lithium ions are inserted/extracted into/from LTO as following so-called topotactic reaction.

$$Li\,[Li_{1/3}Ti^{4+}{}_{5/3}]\,O_4 + Li^+ + e^- \leftrightarrow Li_2\,[Li_{1/3}Ti^{3+}Ti^{4+}{}_{2/3}]\,O_4$$

LTO has reversible capacity of 165 mAh g^{-1} (theoretical capacity : 175 mAh g^{-1}). The plateau is observed at 1.56 V on charge and discharge curves as shown in Fig 1-4. This is about 1.5 V higher than that of graphite.

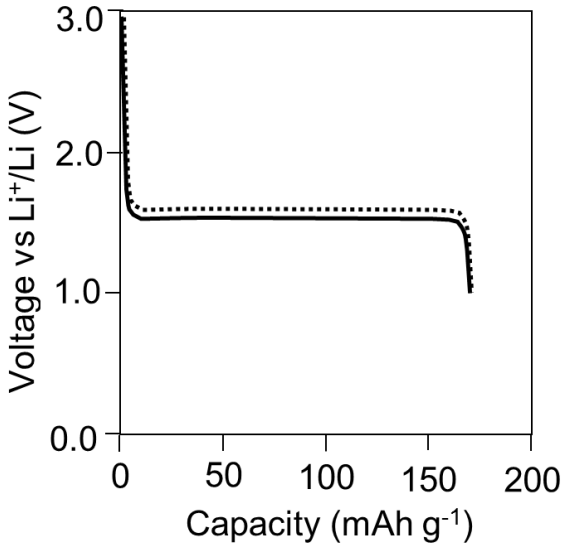

Figure 1-4 Li insertion (solid line) and Li extraction (dotted line) curves of $L_4Ti_{15}O_{12}$ [1-5]

Therefore, a battery fabricated by LTO-anode has lower energy density than a battery fabricated by graphite-anode. On the other hand, this high plateau voltage means that deposition of lithium metal does not occur on the surface of LTO even with high current density. Low energy density of LIB with LTO can be improved by using high-voltage cathode material such as $LiMn_2O_4$, or $Li[Ni_{1/2}Mn_{2/3}]O_4$. In addition, $Li_2[Li_{1/3}Ti^{3+}Ti^{4+}{}_{2/3}]O_4$ shows more superior heat stability than LiC_6. [1-6-7]

Thus, LTO has excellent battery properties except low capacity and consequently. LTO has been used as the anode for mass-produced LIBs.

1-1-2-2 Materials with Alloy-dealloy process

Alloy-dealloy process leads to alloying with lithium by lithium ion absorption and they have large capacity as shown in Fig 1-5. For example, silicon absorbs lithium ion as following reaction, and it forms $Li_{3.75}Si$ alloy. Here, the capacity is 3579 mAh g^{-1} (ten times to the capacity of graphite).

$$Si + 3.75Li^+ + 3.75e^- \leftrightarrow Li_{3.75}Si$$

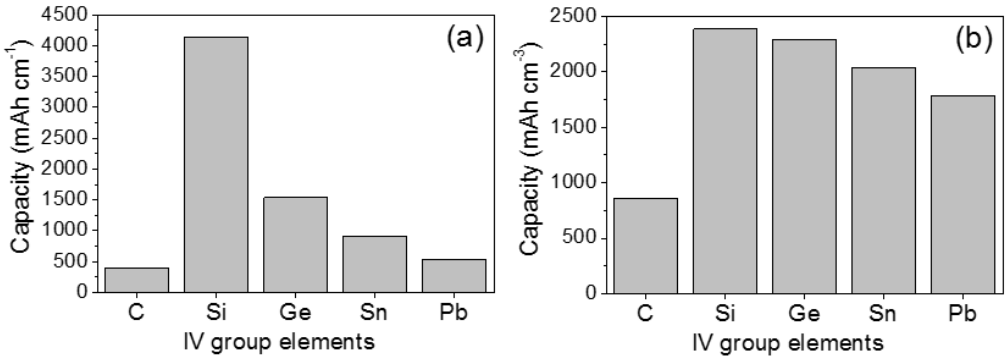

Figure 1-5 Gravimetric (a) and volumetric (b) capacity of Group IV elements and graphite. (C_6Li, $Li_{4.4}Si$, $Li_{4.25}Ge$, $Li_{4.25}Sn$, $Li_{4.25}Pb$) [1-8]

On the other hand, alloy-dealloy process generally shows large volume expansion through absorbing reaction of lithium ion. This large volume change causes disconnection of the active materials electrically and capacity decreasing suddenly. In case of silicon, the capacity decreases from 3500 mAh g^{-1} to 200 mAh g^{-1} by repeating of charge and discharge reaction as shown in Fig 1-6.

Thus, the materials with alloy-dealloy process have higher capacity than graphite, but their poor cycle properties should be one of barriers to adapt them as an anode materials for LIBs.

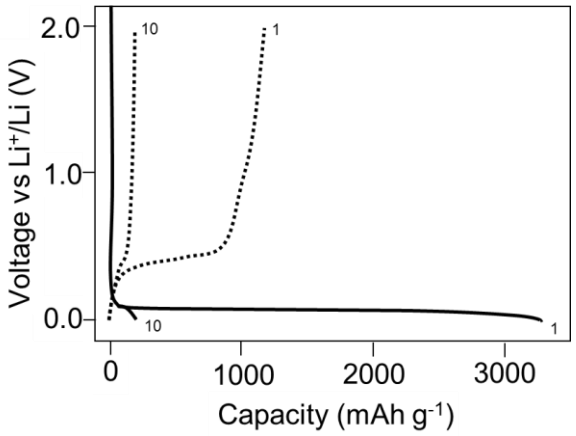

Figure 1-6 Charge (solid line) and discharge (dotted line) curves of slicon [1-9]

1-1-2-3 Conversion reaction materials

Conversion reaction materials as anode materials for LIBs are reported by Poisot, *et al*. in 2000 [1-10]. They revealed that transition metal oxides had large capacity as shown in Fig 1-7. Conversion reactions represent as following reaction,

$$M_xX_y + ne^- + nLi^+ \leftrightarrow xM + yLi_{y/n}X$$

Here, M_xX_y are metal oxides, sulphides, nitrides, phosphides, fluorides and hydrides. Materials for the conversion reactions possess high capacity because two or more electrons per redox centre can be used. However, these materials have poor energy efficiency due to a large polarization between charge and discharge curves. For example, the difference between charge-potential and discharge one is more than 1 V in case of CoO. (Fig. 1-7) According to recent report, hydrides have the smallest polarization and it will be explained particularly in section 1-3.

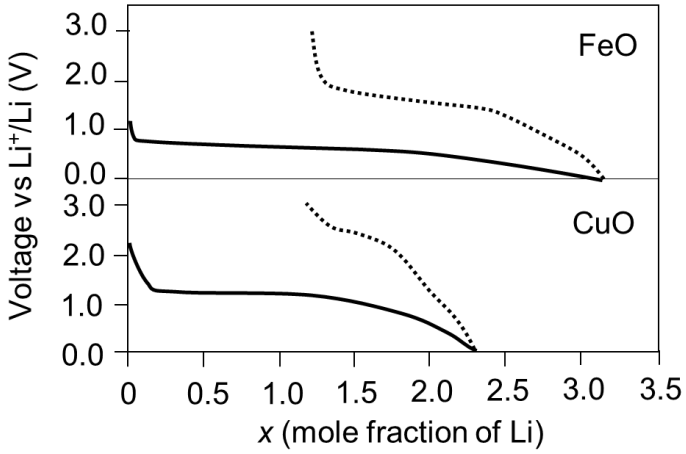

Figure 1-7 Charge-discharge curves of CuO and FeO [1-10-11]

1-1-3 Electrolytes

Fig 1-8 shows schematic open-circuit energy diagram of an aqueous electrolyte. Here, Φ_A and Φ_C are work functions of the anode and cathode and E_g is the energy separation between the lowest unoccupied molecular orbital (LUMO) and the highest occupied molecular orbital (HOMO). The anode is a reductant and the cathode is an oxidant. The anode and cathode should have electronic conductivity. Open circuit voltage V_{oc} can be represented as follows,

$$eV_{OC} = \mu_A - \mu_C.$$

where e is magnitude of the electron charge and μ_A and μ_C are electrochemical potentials of anode and cathode. If μ_A is higher than LUMO, anode should reduce the electrolyte unless solid electrolyte interface (SEI) is created on the surface between electrolyte and anode. On the other hand, if μ_C is lower than HOMO, cathode should oxidize the electrolyte unless SEI is created on the surface between electrolyte and cathode. SEI prevents an electronic transfer from the anode (cathode) to the electrolyte and has an ability of high lithium ionic conductivity.

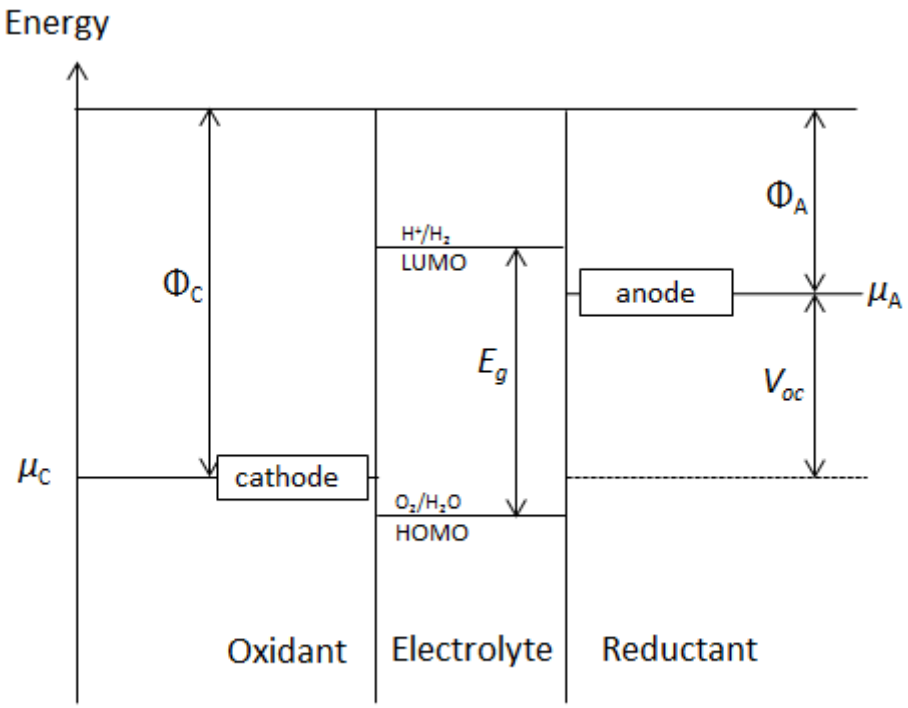

Figure 1-8 Schematic open-circuit energy diagram of an aqueous electrolyte [1-12]

E_g should be larger than eV_{oc} as follows in order to avoid the decomposition of electrolyte,

$$E_g \geqq eV_{oc},$$

In the case of aqueous liquid electrolyte E_g is 1.3V. Therefore, aqueous liquid electrolyte is not adapted on the LIBs system because eV_{oc} of LIBs exceeds 3.4V. Thus, aqueous liquid electrolyte cannot be used as an electrolyte for LIBs. Main requirements of electrolyte for LIBs are as follows,

1) Large potential window over 3.4V ($E_g \geqq eV_{oc}$)
2) A lithium ionic conductivity $\sigma_{Li} > 10^{-4}$ S cm^{-1}
3) An electronic conductivity $\sigma_e < 10^{-10}$ S cm^{-1}
4) A lithium transport number $\sigma_{Li}/\sigma_{total} \cong 1$, where σ_{total} includes conductivities by other ions.

Liquid electrolytes are usually composed of a lithium salt and two or more solvent to meet contradicting requirements of batteries. Cyclic carbonates and linear carbonate have low viscosity, and then the activation energy for lithium diffusion is low. Therefore, they are used commonly as a solvent in a LIB. Typical cyclic and linear carbonates are propylene carbonates (PC), ethylene carbonate (EC), diethyl carbonate (DEC), dimethyl carbonate (DMC), or ethyl methyl carbonate (EMC). Fundamental physical properties of cyclic and linear carbonates solvents are shown in Table 1-1 [1-13]. Here, ε is a dielectric constant, η is a viscosity, T_m is a melting point, T_b is a boiling point, and T_f is a flash point. Today, the mixture of EC with one or more of these linear carbonates [1-14] is used as the electrolyte for commercial LIBs.

$LIPF_6$ has well balanced properties which are conductivity, chemical stability toward moisture, and so on. Hence, $LiPF_6$ has been used since Sony corp. used it for LIBs. Fundamental physical properties of typical lithium salts are shown in Table 1-2 [1-13].

Non-aqueous organic liquid electrolyte is used due to its large potential window in order to realize high density energy of commercial LIBs. On the other hand, this organic electrolyte is usually flammable. Therefore, commercial LIBs possess safety issue potentially.

Table 1-1 Organic cyclic and linear carbonates solvents [1-13]

Solvent	M.Wt	T_m [°C]	T_b [°C]	η/cP 25°C	ε 25°C	Dipole Moment [debye]	T_f [°C]	d [gcm^{-3}] 25°C
EC	88	36.4	248	1.90 (40°C)	89.78	4.61	160	1.321
PC	102	-48.8	242	2.53	64.92	4.81	132	1.200
DMC	90	4.6	91	0.59 (20°C)	3.107	0.76	18	1.063
DEC	118	-74.3	126	0.75	2.805	0.96	31	0.969
EMC	104	-53	110	0.65	2.958	0.89		1.006

Table 1-2 Lithium salts [1-13]

Salt	M.Wt	T_m [°C]	$T_{decomp.}$ [°C] in solution	σ_{25} [S cm^{-1}] (1.0M, in PC)	σ_{25} [S cm^{-1}] (1.0M, in EC/DMC)
$LiBF_4$	93.9	293	>100	3.4×10^{-3}	4.9×10^{-3}
$LiPF_6$	151.9	200	~80 (EC/DMC)	5.8×10^{-3}	10.7×10^{-3}
$LiAsF_6$	195.9	340	>100	5.7×10^{-3}	11.1×10^{-3}
$LiClO_4$	106.4	236	>100	5.6×10^{-3}	8.4×10^{-3}

1-2 Solid electrolytes

All solid state LIBs is composed of non-flammable solid electrolyte instead of flammable non-aqueous liquid electrolyte. Therefore, all solid state LIBs can overcome safety issue of commercial LIBs. Advantages of all solid state LIBs are as follows,

Advantages

- Non-flammable
- None of electrolyte leakage
- None of vapor of electrolytes
- None of phase transition at low temperature
- Long life cycle.

The lithium transport number of the solid electrolyte is equal to 1. Therefore, side reaction with electron or other reactant ion transfer does not occur in all solid state LIBs. This leads to the long life cycle of all solid state LIBs. Furthermore, direct information of the electrode of all solid state LIBs can be obtained after charge or discharge reaction, because it's not necessary to clean the electrode or vaporize liquid electrolyte to measure NMR, XPS, XRD or other spectroscopic analysis. Against these advantages, all solid state LIBs have disadvantage as follows,

Disadvantages

- High resistivity between solid electrolyte and solid active material
- Destroy of interface of solid electrolyte and solid active material
- Low current density and power density.

In order to overcome low current density or low power density, studies of all solid state LIBs mainly have focused on the development of solid electrolytes which have high lithium ionic conductivity. Thus, solid electrolyte is key materials in all solid state LIBs.

There are mainly tree types of solid electrolytes,

Inorganic crystalline and glassy solid electrolytes have sulfide and oxide types. Sulfide electrolytes have higher lithium ionic conductivity than that of oxide electrolytes, because the polarizability of sulfur is larger than that of oxygen. The lithium ionic conductivity of many kinds of electrolytes is shown in Fig 1-9. According to recent reports, $Li_{10}GeP_2S_{12}$ solid electrolyte has higher lithium ionic conductivity than that of liquid electrolytes

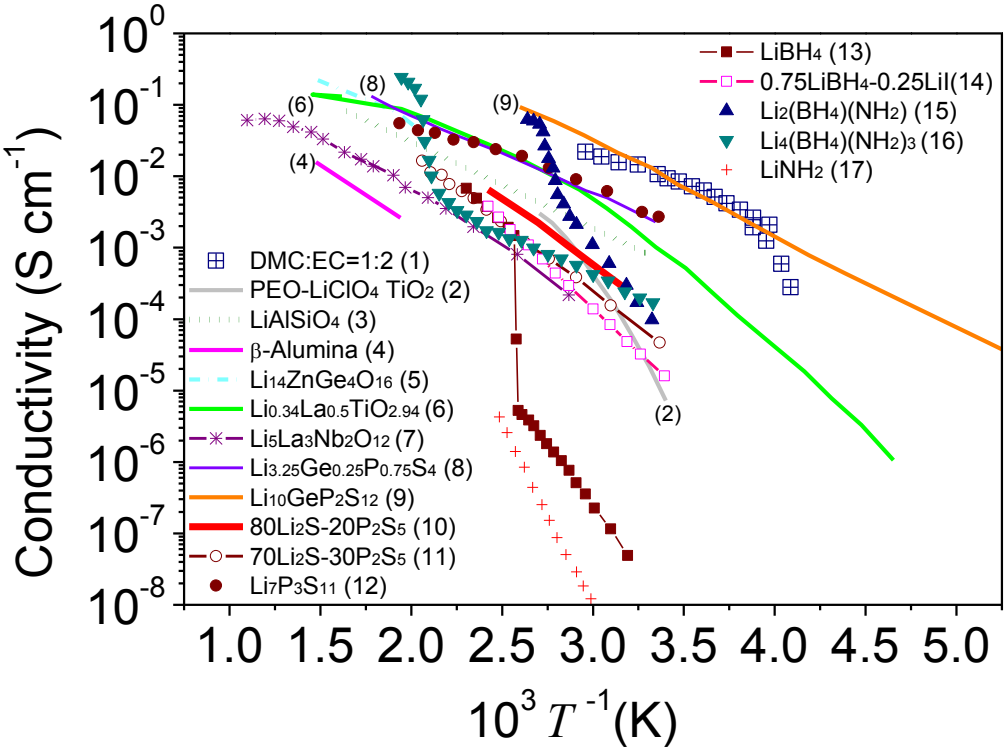

Figure 1-9 Lithium ionic conductivity of electrolytes (solid electrolytes, organic liquid electrolytes, polymer electrolytes, ionic liquids and gel electrolytes) [1-15]

1-2-1 Polymer electrolytes

Polyethylene oxide (PEO) is known as a typical polymer electrolyte, which dissolves into lithium salt (LiTFSI). Generally, it is difficult to recognize lithium ion single conduction in polymer electrolytes because high polymer chain strongly coordinates lithium ion, so the lithium transport number in polymer electrolyte is known to be 0.5 or less. The electrolyte which has low lithium transport number causes large polarization between electrodes, leading to increasing resistance of the electrolyte. Therefore, the research to develop polymer electrolyte which has lithium ion single conduction has been carried out. In addition, the lithium ion conduction couples with segmental motion of polymer in amorphous polymer electrolytes, so lithium ionic conductivity suddenly decreases at around glass transition temperature (T_g), indicating that the segmental motion is frozen. The research to develop decouple-polymer electrolyte should be needed, where lithium ion conduction does not couple with the segmental motion of polymer. The methods of development for decouple-polymer electrolyte which has single lithium ion conduction are shown in Table 1-3.

Table 1-3 Method of development for polymer electrolytes [1-16-21]

Method	Polymer electrolytes	σ_{25} [S cm^{-1}]
Addition of inorganic filler	PEO-$LiClO_4$-TiO_2	10^{-5}
(Urilization of)	PEO-boroxine ring-$LiCF_3SO_2$	10^{-8}
anion-fixed polymer	PEO-borate	10^{-5}
crystalline polymer	PEO-LiAsF6-LiTFSI	10^{-6}
liquid crystal polymer	Liquid crystal polymer-$LiClO_4$	10^{-5}
ionic liquid or molten salt	PRO-LiI-LiOAc-$LiClO_4$-$LiClO_3$	10^{-4}

1-2-2 Inorganic crystalline solid electrolytes

The well-ordered crystal structure supplies proper conductive path for lithium ion diffusion on the inorganic crystalline solid electrolytes. The inorganic crystalline solid electrolyte should have following properties,

1. Possession of conductive path which is recognized as ionic diffusion
2. Disordered sub-lattice which is composed of conductive ions
3. Large polarizability of conductive ions or other ions which compose lattice
4. Possession of proper large bottle neck for ion conductivity.

1-2-2-1 Oxide-based crystalline solid electrolytes

There are many oxide-based crystalline solid electrolytes, such as $LiAlSiO_4$, Li-β-Al_2O_3, LISICON, $La_{2/3-x}Li_{3x}TiO_3$, and $La_3Li_5Nb_2O_{12}$ which have lower lithium ionic conductivity at room temperature as compared with sulfide solid electrolytes. Therefore it is difficult to utilize those as solid electrolyte for all solid state LIBs at room temperature. However, oxide lithium ion conductor is stable even in the ambient atmosphere, so oxide lithium ion conductors will be utilized for thin film all solid state LIBs at room temperature or all solid state LIBs at high temperature of 300 °C or more.

1-2-2-2 Sulfide-based crystalline solid electrolytes

thio-LISICON

The sulfide-based crystalline solid electrolytes which have the same crystal structure as LISICON ($Li_{14}ZnGe_4O_{16}$) is called thio-LISICON. Table 1-4 shows the thio-LISICON system and its conductivity. The fundamental compounds are Li_4SiS_4,

Li_4GeS_4 and Li_3PS_4 on the thio-LISICON system. When Li_4MS_4, Li_3MS_4, and Li_5MS_4 are the stoichiometric composition, solid solution of these compounds shows the highest lithium ionic conductivity at middle composition of solid solution.

$Li_{4-x}Ge_{1-x}P_xS_4$ is typical material of the thio-LISICON system. The lithium ionic conductivity depends on x and shows the highest conductivity of 2.2×10^{-3} and the lowest activation energy at x=0.75 [1-23].

Table 1-4 thio-LISICON system and conductivity [1-22]

System	Compounds	σ_{25} [S cm^{-1}]
Li_2S-GeS_2	Li_4GeS_4	2.0×10^{-7}
Li_2S-GeS_2-ZnS	$Li_{4-2x}Zn_xGaS_4$	3.0×10^{-7}
Li_2S-GeS_2-Ga_2S_3	$Li_{4+x}Ge_{1-x}Ga_xS_4$	6.5×10^{-5}
Li_2S-GeS_2-P_2S_5	$Li_{4+x}Ge_{1-x}P_xS_4$	2.2×10^{-3}
Li_2S-GeS_2-Sb_2S_5	$Li_{4+x}Ge_{1-x}Sb_xS_4$	4.4×10^{-6}
Li_2S-Al_2S_3	$Li_{4+x}Al_xGeS_4$	1.4×10^{-7}
Li_2S-SiS_2	Li_4SiS_4	5.0×10^{-8}
Li_2S-P_2S_5	Li_3PS_4	3.0×10^{-7}
Li_2S-Al_2S_3	Li_5AlS_4	1.5×10^{-9}
Li_2S-SiS_2-Al_2S_3	$Li_{4+x}Si_{1-x}Al_xS_4$	2.3×10^{-7}
Li_2S-SiS_2-P_2S_5	$Li_{4-x}Si_{1-x}P_xS_4$	6.4×10^{-4}

$Li_{10}GeP_2S_{12}$

$Li_{10}GeP_2S_{12}$ has the highest lithium ionic conductivity of 10^{-2} S cm^{-1} at room temperature and the activation energy for lithium ionic conductivity is 24 kJ mol^{-1} for the temperature range from −110 to 110 °C, showing typical activation energy for superionic conductors as shown in Fig.1-10. The conductivity of $Li_{10}GeP_2S_{12}$ is comparable to that of practical organic liquid electrolyte at room temperature. In addition, $Li_{10}GeS_2P_{12}$ exhibits more superior conductivity than that of liquid electrolyte

in low temperature region less than 30 °C. Ceramic conductor is dominant in high temperature region.

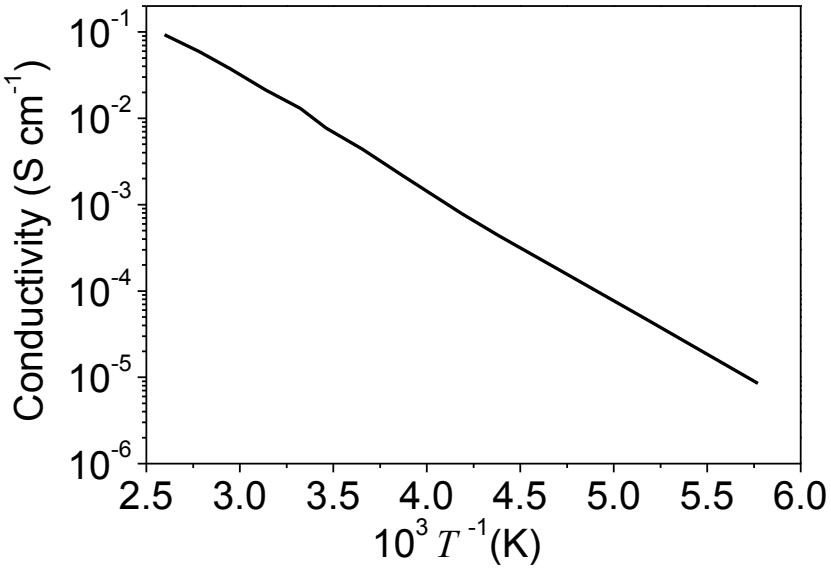

Figure 1-10 Temperature dependence for Li ionic conductivity of $Li_{10}GeP_2S_{12}$ [1-14]

$Li_{10}GeP_2S_{12}$ has one dimensional chain parallel to c-axis formed by LiS_6 octahedral and Ge/PS_4 tetrahedral, which are connected by a common edge. These chains are connected by a common corner with PS_4 tetrahedral and formed three dimensional framework structure as shown in Fig. 1-11. (The crystal structure of $Li_{10}GeP_2S_{12}$ was drawn by VESTA [1-24].) The one dimensional conduction path is formed by LiS_4 tetrahedral parallel to c-axis which is connected by common corners of the LiS_4. Thus, $Li_{10}GeP_2S_{12}$ has new framework structure, forming LiS_6 octahedral and Ge/PS_4 tetrahedral, and lithium exist one dimensional void of framework structure.

It is possible to develop higher lithium ion conductor by controlling the lithium deficient quantities, magnitude of bottleneck, or interstice lithium quantities on the basis of this new framework structure.

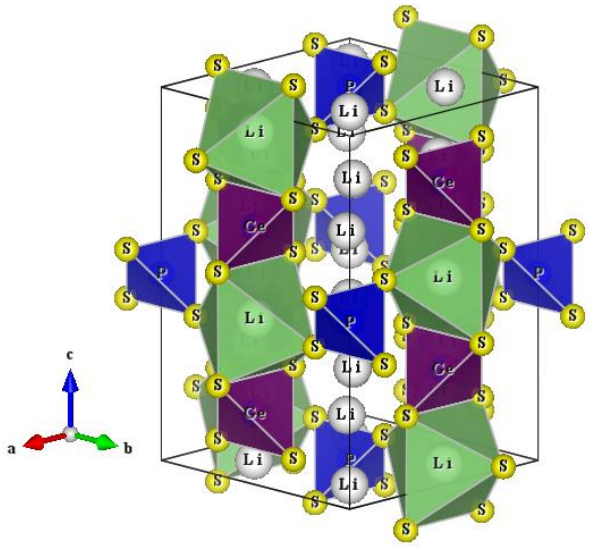

Figure 1-11 Crystal structure of $Li_{10}GeP_2S_{12}$

1-2-2-3 Hydride based solid electrolytes

$LiBH_4$ has been studied as one of candidates for hydrogen storage. Recently, Maekawa,*et al.* reported that $LiBH_4$ exhibits high Li ionic conductivity. $LiBH_4$ shows structural transition from orthorhombic (LT phase) to hexagonal (HT phase) at 115 °C, and its Li ionic conductivity jumps by three orders of magnitude at the temperature as shown Fig.1-9. It is necessary to improve Li ionic conductivity in the LT phase to practical us. Maekawa *et al*. suggested that HT phase stabilize by adding lithium halides, including LiCl, LiBr, and LiI [1-25].

1-2-3 Inorganic glassy solid electrolytes

Polymer electrolytes are worked at temperature of glass transition temperature (T_g) or more as state of super-cooled liquid. Polymer electrolytes have a bridge structure and high lithium ionic conductivity with keeping solid state. The polymer electrolyte is so called couple-electrolyte, so the lithium transport number is 0.5 or less in principle.

On the other hand, inorganic glassy solid electrolytes are utilized at temperature of T_g or less as glassy state. The structure relaxation time of inorganic glassy solid electrolyte is longer than that of polymer electrolyte. The glassy state is solid state and begins to flow macroscopically at more than T_g. The glassy solid electrolyte is so called decouple-electrolyte, namely the lithium transport number is equal to 1. It is known that the conductivity of glassy solid electrolytes is increased by the following factors,

1. Increasing lithium ion concentration
2. Utilization of mixed anion effect
3. Forming metastable phase.

Glassy solid electrolyte is obtained by rapid quenching method or mechanical milling techniques. There are two types of solid electrolyte in glassy solid electrolytes system. One is oxide-based glassy solid electrolyte and the other is sulfide-based glassy solid electrolyte.

1-2-3-1 Oxide-based glassy solid electrolytes

Oxide-based glassy solid electrolytes such as Li_2O-B_2O_3 and Li_2O-SiO_2 systems are usually obtained by rapid quenching method. Generally, the lithium ionic conductivity

of oxide-based glassy solid electrolyte is low. Therefore, oxide-based glassy solid electrolytes is utilized for thin-film all solid state LIBs. Thin-firm oxide solid electrolytes, for example $Li_{3.3}PO_{3.9}N_{0.17}$ and $Li_{3.6}Si_{0.6}P_{0.4}$ which are called LIPON, are synthesized by vapor phase method such as sputtering. Thinning of oxide solid electrolyte makes the effective resistance to be lower, so thin-film all solid state LIBs have been developed and showed good cycle properties.

1-2-3-2 Sulfide-based glassy solid electrolytes

Sulfide-based glassy solid electrolyte such as Li_2S-SiS_2, Li_2S-GeS_2, Li_2S-B_2S_3, and Li_2S-P_2S_5 system are obtained by twin-roller rapid quenching method or melt-rapid-quenching method. These methods need sealed decompression quartz to synthesize binary sulfide glassy solid electrolyte, so these methods have barrier on manufacturing process. Table 1-5 shows lithium ionic conductivity at room temperature of sulfide-based glassy solid electrolyte, and its method of synthesis.

Table 1-5 Conductivity (σ) of sulfide solid electrolytes at room temperature [1-26]

Solid electrolytes	σ [S cm^{-1}]	Method of synthesis
$50Li_2S$-$50GeS_2$	4.0×10^{-5}	Water quenching
Li_2S-B_2S_3	10^{-4}	Water quenching
$50Li_2S$-$50SiS_2$	1.2×10^{-4}	Water quenching
$36Li_2S$-$24SiS_2$-40LiI	1.8×10^{-3}	Liquid N_2 quenching
$42Li_2S$-$28SiS_2$-30LiI	8.2×10^{-4}	Twin-roller quenching
$60Li_2S$-$40SiS_2$	1.5×10^{-4}	Mechanical milling
$66Li_2S$-$33P_2S_5$	10^{-4}	Water quenching
$70Li_2S$-$30P_2S_5$ (glass-ceramic)	3.2×10^{-3}	Glass-ceramic

The lithium ionic conductivity of sulfide-based glassy solid electrolyte can be improved by adding halogenated compound into oxide solid electrolyte, which has large polarizability. Although lithium ionic conductivity of Li_2S-SiS_2 increases by adding LiI, the thermal stability of Li_2S-SiS_2 becomes lowered and reactivity between solid electrolyte and lithium metal is improved by mixing with halogenated compound. Therefore, addition of halogenated compound into Li_2S-SiS_2 is not suitable for application of all solid state LIBs.

On the other hand, lithium ionic conductivity of Li_2S-SiS_2 is increased by adding of small amounts of lithium ortho-oxosalts such as Li_3PO_4 or Li_4SiO_4. These oxysulfide glasses have large voltage window of 10V and more, and the lithium transport number is equal to 1. The $Si_2O_6^{6-}$ ion exists in oxysulfide glasses and this $Si_2O_6^{6-}$ ion consists of one bridging oxygen and six non -bridging sulfide. Non-bridging oxygen usually traps lithium ion and leads to decreasing of lithium ionic conductivity. However, the bridging oxygen only traps lithium ion weekly. In addition, bottleneck is expanded by doping oxygen. These lead to high lithium ionic conductivity of oxysulfide glasses.

Li_2S-SiS_2 and Li_2S-P_2S_5 are also obtained by mechanical milling technique. Mechanical milling technique proceeds at room temperature and ambient atmosphere, so it is easy to treat even sulfide which has high vapor pressure at thigh temperature. In addition, both of mechanical milling technique and melt-rapid-quenching method supply Li_2S-P_2S_5 or Li_2S-SiS_2, which have the same local structure and the same lithium ionic conductivity. Moreover, the glassy solid electrolyte which is synthesized by mechanical milling has already become fines, so this solid electrolyte can be utilized for all solid state LIBs without any other procedures.

The lithium transport number of Li_2S-P_2S_5 is 1. In addition, Li_2S-P_2S_5 has large potential window of 5V and more. The Lithium ionic conductivity of Li_2S-P_2S_5 system was improved mostly by heat treatment. Glass-ceramic phase is precipitated by heat treatment on the Li_2S-P_2S_5 system. This glass-ceramic phase is metastable phase and this new crystal phase is not obtained ordinary by solid-solid reaction of Li_2S and P_2S_5.

$80Li_2S$-$20P_2S_5$ shows the highest lithium ionic conductivity of 2.1×10^{-4} S cm^{-1} and further increasing of mol percent of Li_2S brings decreasing of conductivity. The activation energy is about 35 kJ mol^{-1} and does not depend on the mol percent of Li_2S. The lithium ionic conductivity of Li_2S-P_2S_5 glasses is improved by heat treatment except in case that the mol percent of Li_2S is 67. The composition dependence of activation energy for glass-ceramics exhibits good corresponding relationship.

Glass ceramic of $70Li_2S$-$30P_2S_5$ has the highest lithium ionic conductivity of 3.2×10^{-3} S $cm^{-1}$and the lowest activation energy of 12 kJ mol^{-1}. $80Li_2S$-$20P_2S_5$ also shows increasing of lithium ionic conductivity by heat treatment from 2.1×10^{-4} S cm^{-1} to 1.3×10^{-4} S cm^{-1}.

The differences of the magnitude of lithium ionic conductivity of Li_2S–P_2S_5 glass-ceramics were explained by precipitated crystalline phases in the glass-ceramics. According to the XRD profile of xLi_2S-(1-x) P_2S_5 (x=67, 70, 75, 80 and 87.5 mol percent), $67Li_2S$-$33P_2S_5$ exhibits decreasing of lithium ionic conductivity by heat treatment due to precipitation of stable phase of $Li_4P_2S_6$. $Li_4P_2S_6$ crystal has been reported to have low lithium ionic conductivity of 10^{-7} S cm^{-1} or less at room temperature. Thio-LISICON II analog phase of $Li_4Ge_2S_4$-Li_3PS_4 system pattern is observed at x=80. Similarly, Thio-LISICON III analog phase is observed at x=87.5. Thio-LISICON II has higher lithium ionic conductivity than that of thio-LISICON III.

This is reason why $80Li_2S$-$20P_2S_5$ glass ceramic has higher lithium ionic conductivity than that of $87.5Li_2S$-$12.5P_2S_5$. On the other hand, new crystal phase is observed at x=70.

The local structure of $70Li_2S$-P_2S_5 glass ceramic, $80Li_2S$-$20P_2S_5$ glass ceramic, and the thio-LISICON II ($Li_{3.25}Ge_{0.25}P_{0.75}S_4$) are investigated by Raman spectroscopic measurement [1-27]. The main band at 410 cm^{-1} and 425 cm^{-1} are corresponding to the $P_2S_7^{4-}$ (pyro-thiophosphate) and PS_4^{3-} (ortho-thiophosphate), respectively [1-28]. $80Li_2S$-$20P_2S_5$ glass ceramic has the band of PS_4^{3-} which is observed in thio-LISICON II. $70Li_2S$-$30P_2S_5$ glass ceramic has both band of PS_4^{3-} and $P_2S_7^{4-}$. Thus, PS_4^{3-} and $P_2S_7^{4-}$ ions are very important role to enhance the conductivities of glass ceramics of Li_2S-P_2S_5 system.

1-3 Magnesium hydride

1-3-1 Magnesium hydride for lithium ion batteries

Recently, Oumellal *et al.* demonstrated the anode properties of MgH_2 for LIBs experimentally. MgH_2 has potential as a LIB anode, showing 2038 mA h g^{-1} as the theoretical capacity [1-29-30].The voltage-composition (x: mole fraction of Li) curve of MgH_2 has two plateau as shown in Fig 1-12. According to the XRD patterns, the starting material is consistent with MgH_2. As MgH_2 react with lithium ion, the intensity corresponding to the peak of MgH_2 peak decreases, on the other hand, the intensity corresponding to two peaks of magnesium (Mg) and lithium hydride (LiH) increases and reaches their maximum around x=2.0. This suggests that Mg react with lithium ion by the following conversion reaction on the first plateau at 0.5V,

$$MgH_2 + 2Li^+ + 2e^- \leftrightarrow Mg + 2LiH.$$

Afterwards, Mg reacts with lithium ion and transforms into the hcp-type lithium-magnesium alloy (Li_3Mg_{17}) and bcc-type lithium-magnesium alloy (Li_3Mg_7) by the following alloy-dealloy reaction on the second plateau at 0.1V and the sloping voltage curve from x=2.5 to 2.9.

$$Mg + yLi^+ + ye^- \leftrightarrow Li_yMg$$

The reversibility of the MgH_2 is shown in the inset of Fig 1-22. The charge capacity (the number of lithium extraction) is 4000 mAh g^{-1} and the discharge capacity (the number of lithium insertion) is 2700 mAh g^{-1}, so the coulombic efficiency is 68%, where the coulombic efficiency is equal to the charge capacity divided by the discharge capacity. This means that 32% of inserted lithium ion remains the electrode.

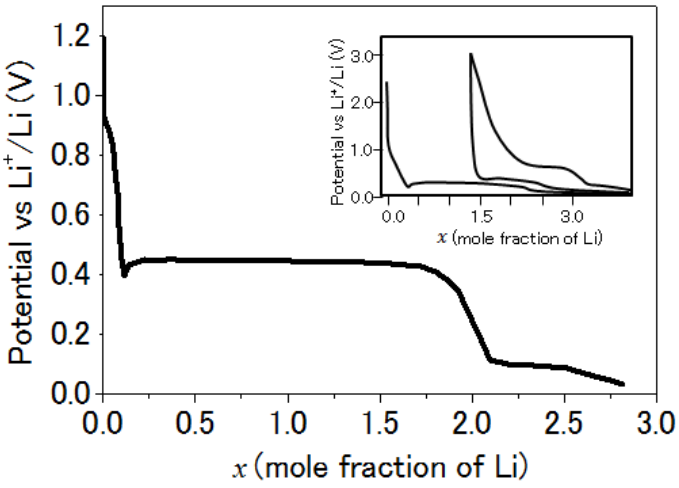

Figure 1-12 Voltage composition curve of MgH_2 on the lithium insertion reaction between 0.005V and 3.0V at a rate of one lithium in 100h.

Inset : The voltage composition curve on the lithium insertion and extraction reaction as a function of *x* at rate of one lithium in 10h [1-29].

The large first coulombic efficiency is improved by the ball milling procedure of MgH_2 and limited the lithium insertion/extraction reaction as conversion reaction as shown in Fig 1-13. The coulombic efficiency increases from 68% to 75% and the reversible capacity 1480 mAh g^{-1}. The reversible capacity decreases suddenly with the increasing cycle numbers when the first capacity is 1480 mAh g^{-1} as shown the inset of Fig. 1-13 (red line). On the other hand, the battery cell remains reversible capacity of 520 mAh g^{-1} after 50 cycle test when the constrained first reversible capacity is 800 mAh g^{-1} by limiting the reaction as shown in the inset of Fig. 1-13 (blue line).

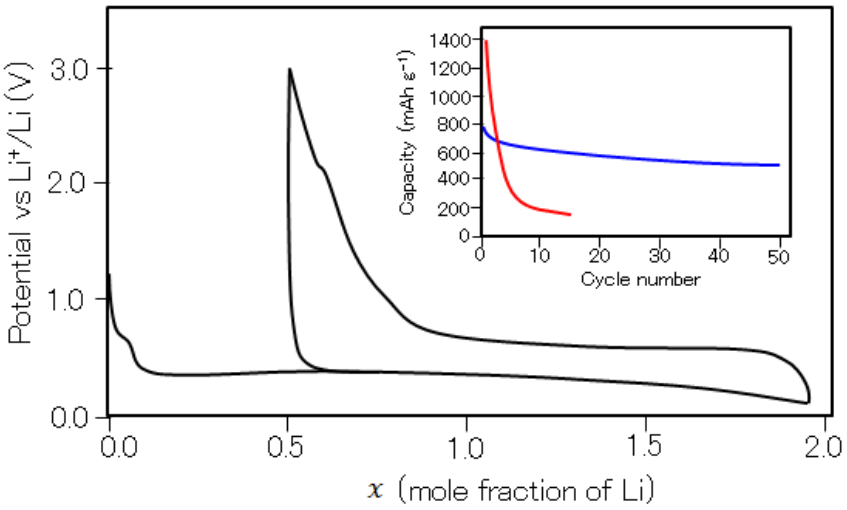

Figure 1-13 Voltage composition curve of MgH_2 on the lithium insertion reaction between 0.15V and 3.0V at a rate of one lithium in 10h. Inset : Reversible capacity versus the cycle number between 0.15V and 2.5V. [1-29]

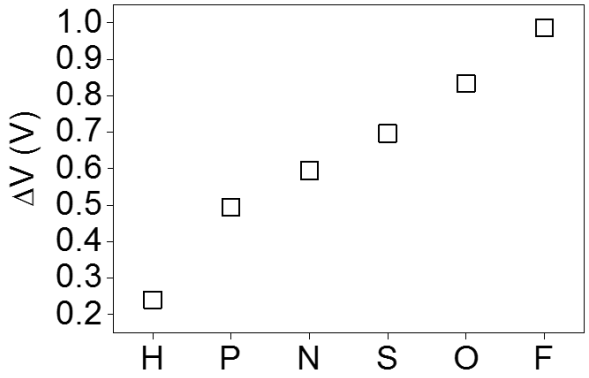

Figure 1-14. Charge and discharge polarization of conversion materials [1-29]

According to the comparison betwee the MgH_2 and other anode materials of coversion reaction, for example, covalt based fluorides (CoF_3), oxides (CoO), suphides (CoS) or phosphides (CoP_2), the MgH_2 anode showed low polarization during the electrode conversion. Namely, the charge and discharge polarization (ΔV) show the smallest value in MgH_2 electrode as shown in Fig 1-14. This polarization usually originates from poor mass transport kinetics and the H^- ions are expected to diffuse faster than the O^{2-} or F^- ions, therefore MgH_2 shows low polarization.

1-3-2 Magnesium hydride for hydrogen storage

Magnesium (Mg) is light element (24.305 g mol^{-1}) and magnesium hydride (MgH_2) has high hydrogen storage capacity of 7.6 mass%. This capacity is quite high compared to other metal hydrides as shown in Table 1-6. Furthermore, Mg exists abundantly on the Earth. Therefore, magnesium hydride is one of the promising hydrogen storage materials.

Table 1-6 Metal hydride and their hydrogen storage capacity [1-31]

Type	Metal	Hydride	mass%
Elemental	Mg	MgH_2	7.6
Elemental	Pd	$PdH_{0.6}$	0.56
AB_5	$LaNi_5$	$LaNi_5H_6$	1.37
AB_2	ZrV	$ZrV_2H_{5.5}$	3.01
AB	FeTi	$FeTiH_2$	1.89
A_2B	Mg_2Ni	Mg_2NiH_4	3.59
BCC	TiV_2	TiV_2H_4	2.6

Mg has hexagonal close-packed structure. Although Mg does not form hydrogen solid solution, Mg reacts with hydrogen then transforms into hydride as follows,

$$Mg + \frac{1}{2} H_2 \leftrightarrow MgH_2.$$

MgH_2 is insulator with ionic bond and have large negative enthalpy, so the equilibrium pressure for hydrogen ab/desorption is quite low even in the room temperature region. Moreover, the slow kinetics of hydrogen ab/desorption, and therefore requirement of a high temperature of more than 300 °C on the reaction of hydrogen ab/desorption have been barriers to the practical use of MgH_2 as a hydrogen storage material.[1-32,33] By adding a transition metal and metal oxide as a catalyst, the hydrogen sorption kinetics has been improved.[1-34-37] Barkhordarian *et al.* clarified that niobium oxide (Nb_2O_5) was the most effective catalyst among other metal oxides (such as Fe_3O_4, V_2O_5, Mn_2O_5, and so on) to improve the kinetics of the hydrogen ab/desorbing reaction.[1-38-40] as shown in Fig. 1-28. The addition of Sc_2O_3, Al_2O_3, CuO, and SiO_2 causes little change of the desorption rate. Al_2O_3 and SiO_2 have no accelerating improvement on the hydrogen

desorption reactions. On the other hand, the transition metal oxides (Nb_2O_5, Fe_3O_4, V_2O_5, Mn_2O_3, Cr_2O_3, and TiO_2) improve slow kinetics of MgH_2, drastically [1-36].

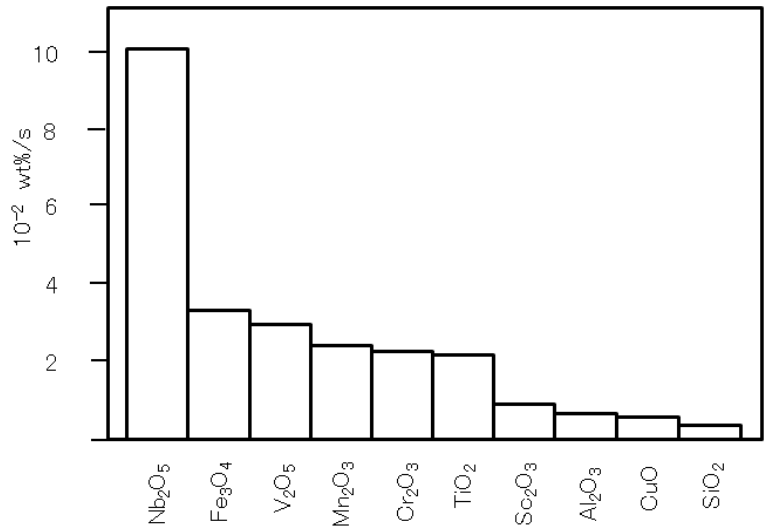

Figure 1-15 Desorption rates of MgH_2 with different metal oxide catalyst at 300 °C into vacuum [1-36]

Barkhordarian *et al.* reported the effect of Nb_2O_5 concentration on the kinetics of the magnesium hydrogen sorption reaction, and they also showed the content dependence of activation energy for the desorption reaction as shown in Fig 1-16. Obviously, the activation energy varies exponentially with the Nb_2O_5 content and reaches a limit of 62 kJ mol^{-1} at 0.2 mol% Nb_2O_5. [1-38-40]

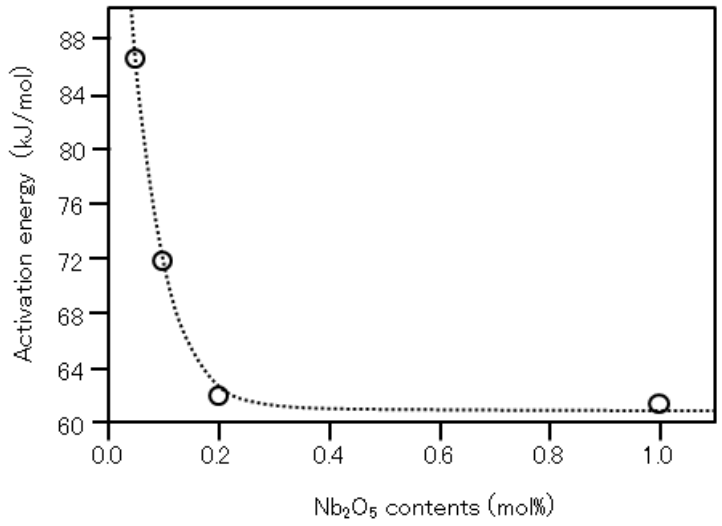

Figure 1-16 Activation energy as a function of Nb_2O_5 content [1-39]

Moreover, Hanada *et al*. reported that the Nb_2O_5-catalyzed MgH_2 was rehydrogenated even at room temperature [1-41-42] as shown in Fig 1-17.

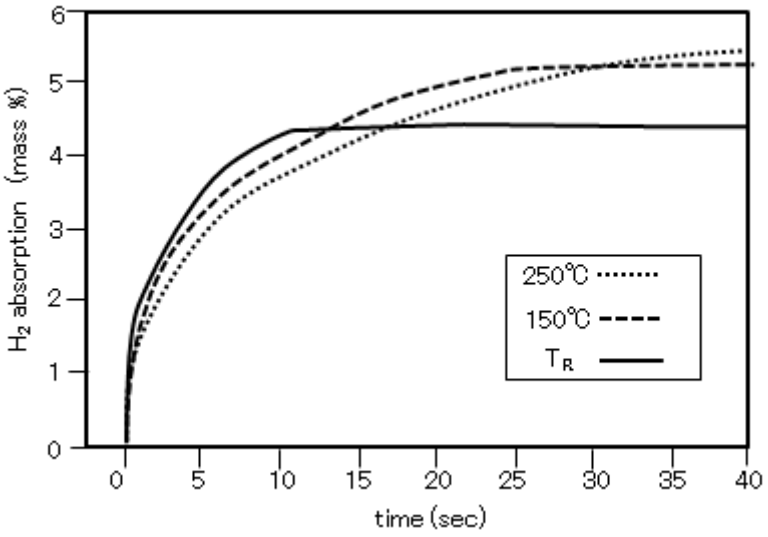

Figure 1-17 Amount of hydrogen absorption as a function of reaction time for the catalyzed Mg at room temperature T_R (~20 ◦C), 150 and 250 ◦C under 1MPa hydrogen

References

[1-1] J. M. Tarascon and M. Armand, *Nature*, 2001, **414**, 359-367.

[1-2] K. Gotoh, M. Maeda, A. Nagai, A. Goto, M. Tansho, K. Hashi, T. Shimizu and H. Ishida, *Journal of Power Sources*, 2006, **162**, 1322-1328.

[1-3] Z. Ogumi and M. Inaba, *Bulletin of the Chemical Society of Japan*, 1998, 71, 521-534.

[1-4] K. M. Colbow, J. R. Dahn and R. R. Haering, *Journal of Power Sources*, 1989, 26, 397-402.

[1-5] T. Ohzuku, A. Ueda and N. Yamamoto, *Journal of The Electrochemical Society*, 1995, **142**, 1431-1435.

[1-6] K. Ariyoshi, R. Yamato and T. Ohzuku, *Electrochimica Acta,* 2005, 51, 1125-1129.

[1-7] J. Jiang, J. Chen and J. R. Dahn, *Journal of The Electrochemical Society*, 2004, 151, A2082-A2087.

[1-8] C.-M. Park, J.-H. Kim, H. Kim and H.-J. Sohn, *Chemical Society Reviews*, 2010,39, 3115-3141.

[1-9] J. H. Ryu, J. W. Kim, Y.-E. Sung and S. M. Oh, *Electrochemical and Solid-State Letters*, 2004, 7, A306-A309.

[1-10] P. Poizot, S. Laruelle, S. Grugeon , L.Dupont and J.-M. Tarascon, *Nature*, 2000, **407**,496-499.

[1-11] P. Poizot, S. Laruelle, S. Grugeon , and J.-M. Tarascon, *Journal of The Electrochemical Society*, 2002, **149**, A1212-A1217.

[1-12] J. B. Goodenough and Y. Kim, *Chemistry of Materials*, 2009, **22**, 587-603.

[1-13] K. Xu, *Chemical Reviews*, 2004, **104**, 4303-4418.

[1-14] J. M. Tarascon and D. Guyomard, *Solid State Ionics*, 1994, **69**, 293-305.

[1-15] N. Kamaya, K. Homma, Y. Yamakawa, M. Hirayama, R. Kanno, M. Yonemura, T. Kamiyama, Y. Kato, S. Hama, K. Kawamoto and A. Mitsui, *Nature Materials*, 2011, 10, 682-686.

[1-16] F. Croce, G. B. Appetecchi, L. Persi and B. Scrosati, *Nature*, 1998, **394**, 456-458.

[1-17] M. A. Mehta and T. Fujinami, *Solid State Ionics*, 1998, **113-115**, 187-192.

[1-18] T. Aoki, A. Konno and T. Fujinami, *Journal of The Electrochemical Society*, 2004, **151**, A887-A890.

[1-19] A. M. Christie, S. J. Lilley, E. Staunton, Y. G. Andreev and P. G. Bruce, *Nature*, 2005, **433**, 50-53.

[1-20] C. T. Imrie, M. D. Ingram and G. S. McHattie, *The Journal of Physical Chemistry B*, 1999, **103**, 4132-4138.

[1-21] C. A. Angell, C. Liu and E. Sanchez, *Nature*, 1993, **362**, 137-139.

[1-22] THE ELECTROCHEMICAL SOCIETY OF JAPAN, THE COMMITTEE OF BATTERY TECHNOLOGY, *Hand book of batteries*, 2010, Ohmsha (Japanese).

[1-23] R. Kanno and M. Murayama, *Journal of The Electrochemical Society*, 2001, 148, A742-A746.

[1-24] K. Momma and F. Izumi, *Journal of Applied Crystallography*, 2011, 44, 1272-1276.

[1-25] H. Maekawa, M. Matsuo, H. Takamura, M. Ando, Y. Noda, T. Karahashi and S. Orimo, Journal of the American Chemical Society, 2009, 131, 894-895.

[1-26] K. Takada, *Acta Materialia*, 2013, 61, 759-770.

[1-27] F. Mizuno, A. Hayashi, K. Tadanaga and M. Tatsumisago, *Solid State Ionics*, 2006, **177**, 2721-2725.

[1-28] M. Tachez, J.-P. Malugani, R. Mercier and G. Robert, *Solid State Ionics*, 1984, 14, 181-185.

[1-29] Y. Oumellal, A. Rougier, G. A. Nazri, J. M. Tarascon and L. Aymard, *Nature Materials*, 2008, 7, 916-921.

[1-30] Y. Oumellal, A. Rougier, J. M. Tarascon and L. Aymard, *Journal of Power Sources*, 2009, 192, 698-702.

[1-31] L. Schlapbach and A. Zuttel, *Nature*, 2001, 414, 353-358.

[1-32] B. Vigeholm, J. Kjoller and B. Larsen, *Journal of the Less Common Metals*, 1980, 74, 341-350.

[1-33] B. Vigeholm, J. Kjoller, B. Larsen and A. S. Pedersen, Journal of the Less Common Metals, 1983, 89, 135-144.

[1-34] G. Liang, J. Huot, S. Boily, A. Van Neste and R. Schulz, *Journal of Alloys and Compounds*, 1999, 292, 247-252.

[1-35] A. Zaluska, L. Zaluski and J. O. Ström-Olsen, *Journal of Alloys and Compounds*, 1999, 288, 217-225.

[1-36] W. Oelerich, T. Klassen and R. Bormann, *Journal of Alloys and Compounds*, 2001, 315, 237-242.

[1-37] N. Hanada, T. Ichikawa and H. Fujii, *The Journal of Physical Chemistry B,* 2005, 109, 7188-7194.

[1-38] G. Barkhordarian, T. Klassen and R. Bormann, *Scripta Materialia*, 2003, 49, 213-217.

[1-39] G. Barkhordarian, T. Klassen and R. Bormann, *Journal of Alloys and Compounds*, 2004, 364, 242-246

[1-40] G. Barkhordarian, T. Klassen and R. Bormann, *Journal of Alloys and Compounds*, 2006, 407, 249-255

[1-41] N. Hanada, T. Ichikawa, S. Hino and H. Fujii, *Journal of Alloys and Compounds*, 2006, 420, 46-49

[1-42] N. Hanada, T. Ichikawa and H. Fujii, *Journal of Alloys and Compounds*, 2007, 446-447, 67-71.

2 Purpose

All solid state lithium ion batteries are safer than commercial lithium ion batteries due to having non-flammable solid electrolyte instead of flammable liquid electrolyte. LIBs will be utilized for many applications more and more in the future society. Therefore, safety and high capacity is one of the most important issues for future market demands in both of stationary and mobile LIBs. All solid state lithium ion batteries could give solution against safety issue, at the same time, the experimental investigation using an all solid state electrolyte should provide more detailed information of the electrode materials before and after the electrochemical reactions compared with liquid electrolytes, because a special treatments prior to some analytical measurements are not necessary. In addition, MgH_2 is one of the most promising candidates as high-capacity anode materials. Although, MgH_2 is also known as a candidate of hydrogen storage material, extremely low reaction speed of hydrogen absorption and desorption has been one of barriers to practical use. Effect of metal oxide additives on hydrogen ab/desorption kinetics of MgH_2 has been examined so far and it is well known that hydrogen ab/desorption kinetics is improved by adding transition metal and metal oxide.

In this thesis, anode properties of MgH_2 with the all solid state lithium ion battery cell are investigated. In particular, the relationship between the hydrogen desorption properties and electrochemical properties of MgH_2 is focused on to improve battery properties of LIBs. It has been well known that metal oxides improve the hydrogen ab/desorbing properties of MgH_2. The purpose of this thesis is to clarify the role of additive metal oxide, Nb_2O_5 and Al_2O_3, to MgH_2 for all solid state LIBs. Generally, Nb_2O_5 drastically improve the slow kinetics of MgH_2. Whereas, Al_2O_3 have no clear

improvement on the hydrogen desorption reactions. A development of the method to fabricate the experimental all solid state LIBs with MgH_2 is also important in this thesis and clarification of fundamental anode properties of MgH_2 will be attempted for the first time.

The fundamental anode properties of MgH_2 are taken up in section 1 of chapter 4. The effect of additive metal oxide to anode properties of MgH_2 is takes up in section 2 of chapter 4. Nb_2O_5 and Al_2O_3 doped MgH_2 are synthesized by planetary ball-milling apparatus. The hydrogen desorption properties of Nb_2O_5 and Al_2O_3 doped MgH_2 are investigated by thermal gas desorption analyses. The charge and discharge reaction are examined to lithium ion insertion and extraction properties of MgH_2. XRD and XPS is carried out to examine structural change and chemical bonding state with lithium insertion and extraction reactions, respectively. Furthermore, ^{27}Al-MAS-NMR is carried out to clarify the local structure of aluminum.

3 Experimental procedures

3-1 Sample preparation

3-1-1 Materials

Pristine materials of this work are shown in Table 3-1. All the samples were handled in a glove-box (Miwa MFG, MP-P60W) filled with a purified Ar (> 99.9999 %) to avoid an oxidation and pollution due to water.

Table 3-1 General information of materials

Materials	Purity, State	Company
Magnesium hydride	98% powder	Alfa Aesar
Niobium oxide	99.5% powder	Sigma Aldrich
Aluminum oxide	99%	Sigma Aldrich
Lithium sulfide	99.9% powder	Furuuchi Chemistry
Phosphorus pentasulfide	99% powder	Sigma Aldrich
Lithium	99% foil	Honjo Metal

3-1-2 Mechanical ball-milling method

Mechanical ball-milling method is one of alloying method, which gives mechanical energy into samples, then the synthesized product may sometimes be in a metastable phase. In particular, planetary ball milling can give stronger physical energy into samples than the other mechanical milling methods, and therefore it has been utilized for various purposes, such as, synthesis of alloy, synthesis of amorphous material, dispersion of catalyst, and so on.

3-1-3 Synthesis of Nb_2O_5 and Al_2O_3 doped MgH_2

Two kinds of oxide doped doped MgH_2 which were (1-*y*)MgH_2-*y*Nb_2O_5 and (1-*z*)MgH_2-*z*Al_2O_3, were synthesized by planetary ball-milling apparatus (Fritsch, P7) as shown in Fig. 3-1. The mixture of Nb_2O_5 (or Al_2O_3) and MgH_2 with the appropriate molar ratios were put into the aluminum milling vessel which is specially designed and made of Cr steel (UMETOKU Co. Ltd., SKD-11) and has an inner volume of about 30 cm^3 with 20 pieces of steel balls with 7mm in diameter. All the procedures were carried out in the glove-box to avoid oxidation and pollution due to moisture. Then, the mixture was mechanically milled for 20 h at 370 rpm under 0.1 MPa of Ar gas atmosphere.

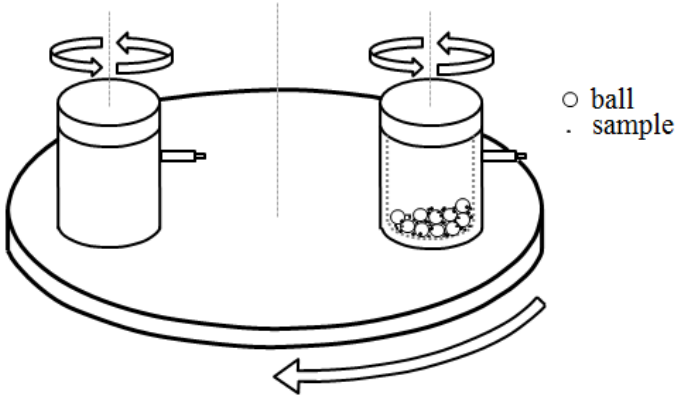

Figure 3-1 Schematic picture of planetary ball milling apparatus (Fritsch P7) [3-2]

3-1-4 Synthesis of solid electrolyte

The solid electrolyte 80Li_2S-20P_2S_5 was synthesized through following procedures [3-1]. The mixture of lithium sulfide (Li_2S) and phosphorus pentasulfide (P_2S_5) with the molar ratios of 80 : 20 were put into alumina mortar to pre-mixing at 50 rpm for 1 hours by automatic magnetic mixing machine. After that, mixed Li_2S-P_2S_5 was put into the zirconia vessel (250 ml internal volume) with 45 pieces of zirconia balls with 8mm in

diameter. All the procedures were carried out in the glove-box to avoid oxidation and pollution due to moisture. Then, the mixture was mechanically milled for 20 h at 370 rpm under 0.1 MPa of argon gas atmosphere using a planetary ball milling apparatus (Fritsch P6) as shown in Fig 3-2.

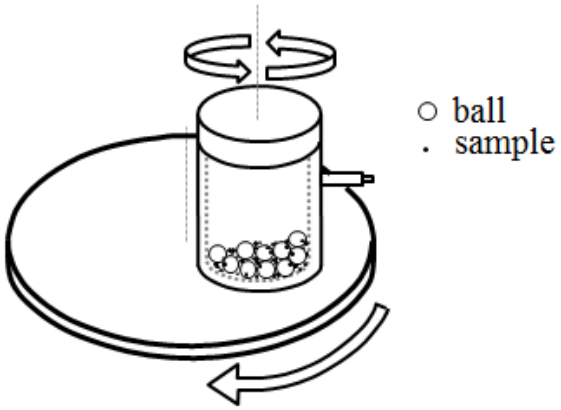

Figure 3-2 Schematic picture of planetary ball milling apparatus (Fritsch P6)

3-2 Experimental technique

3-2-1 Thermogravimetry - Differential Thermal Analysis (TG-DTA)

Principle

Thermal properties of samples are investigated by thermogravimetry (TG) and differential thermal analysis (DTA) as shown in Fig. 3-4. TG is the technique to monitor the weight change of the sample as a function of temperature or time during increasing or decreasing temperature. For example, the weight loss due to the gases desorption from the sample can be detected as a difference between the sample and reference weights as a function of the temperature or the time during the temperature increase. DTA is the technique to monitor the difference in temperature due to melting, phase transition, and/or gases desorption between the samples and reference weights as a function of the temperature or the time during increasing or decreasing of temperature. DTA is carried

out with TG at the same time [3-2]. The desorbed gases are led to an apparatus of thermal desorption mass spectroscopy through the capillary by following He gas as a carrier.

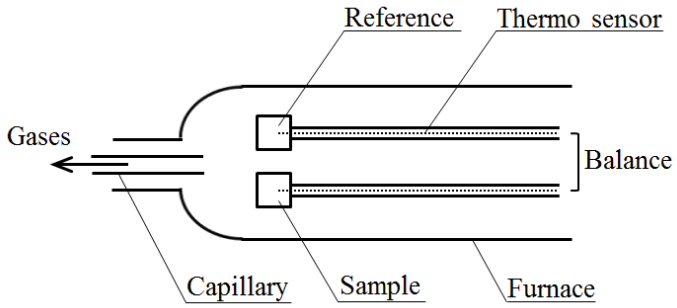

Figure 3-4 TG-DTA apparatus

3-2-2 Thermal desorption mass spectroscopy (TDMS)

Principle

Thermal desorption mass spectroscopy (TDMS) is one of gases analysis methods which provide the information of the desorbed gases from heated sample quantitatively and qualitatively. The TDMS apparatus is connected to the TG-DTA apparatus. The apparatus is composed of three parts which were an ionization source, a quadruple mass spectrometer, and a detector as shown in Fig. 3-5. Here, the inside of the TDMS apparatus is maintained highly vacuumed by turbomolecular pump. The desorbed gas molecules from the sample lost an electron by ion-beam, as a result, the molecule is ionized in ionization part. The ionized gas molecules can be identified by m/z, where m is mass of sample, z is charge number of usually 1 or 2. After that, the ionized molecules are separated by difference of the mass in the quadruple electric field, then mass spectroscopic information can be obtained.

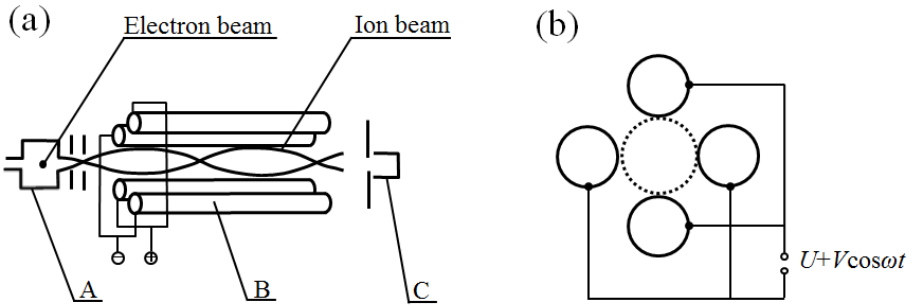

Figure 3-5 (a) TDMS apparatus [3-3] (A: ionization source, B: quadruple mass spectrometer C: detector), (b) Quadruple mass spectrometer

The quadruple mass spectrometer consists of two twin electrodes, which supply a modulated voltage V_m, where V_m is composed of direct current voltage (U) and high frequency voltage ($V\cos\omega t$) as shown Fig.3-5(b). The only ionized molecule having specific m/z can pass through the electrodes with specific voltage V. Thus, the ionized molecule is separated by the mass number. After that, the separated ions are detected as ionic current in detector. (part of C in Fig.3-5(a))

Procedure

The hydrogen desorption temperature of doped Nb_2O_5 or Al_2O_3 MgH_2 were examined by the TDMS apparatus (Anelva, M-QA200TS) connected to the TG-DTA apparatus (Rigaku, TG8120) where they are installed inside the glove-box to avoid exposure of air and moisture. In the TG-DTA-TDMS system, high purity He or Ar gas is flowed as a carrier gas. The heating rate was fixed to be 5 °C/min up to 500 °C from room

temperature. About 5~10 mg of the sample was put into an aluminum pan and set to the balance in the TG-DTA apparatus.

3-2-3 Powder X-ray diffraction (XRD) measurement

Principle

X-ray is one of electromagnetic waves and its wave length is on the same degree with lattice spacing of crystals. The diffraction phenomenon is caused when the wave length of the incident X-ray, λ satisfies the following equation, namely, Bragg low,

$$n\lambda = 2d_{hkl}sin\theta,$$

where d_{hkl} (hkl are Miller indexes) is the distances between plane P_1 and P_2 corresponding to lattice space of crystal and optical path between P_1 and P_2 is equal to $d_{hkl}\sin\theta$ as shown in Fig.3-6. Therefore, X-ray has been utilized for powder X-ray diffraction measurement in order to obtain information of crystal structure.

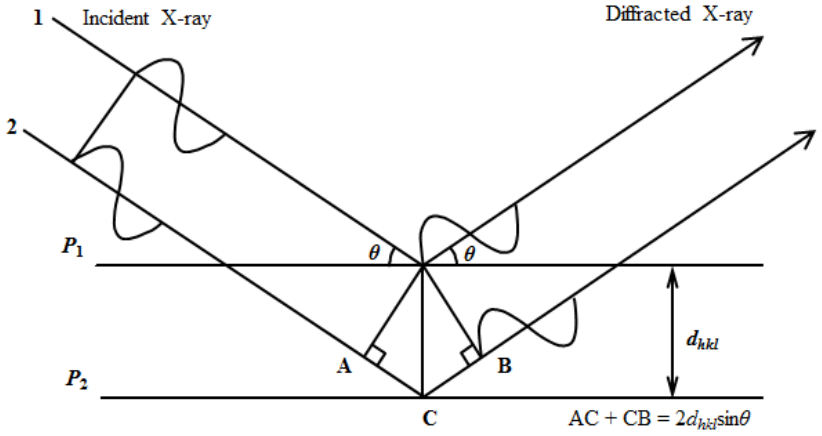

Figure 3-6 Diffraction of X-ray from lattice planes in crystal [3-4]

Procedure

In this work, XRD measurement was carried out to determine the crystal structures of the samples thorough lithium insertion and extraction reactions by the XRD equipment (Rigaku, RINT-2100), in which the X-ray source is Cu-Kα (λ = 0.154 nm) and the energy output is 8 kW (40 kV – 200 mA). A sample was set on the glass and covered with a polyimide sheet (Kapton®, Du Pont-Toray Co. Ltd.) of 8 μm thickness in glove-box. Polyimide sheet touched glass plate with high vacuum grease (Apiezon®, M&I Material Ltd.) to avoid exposure of air and moisture. The obtained XRD patterns were analyzed by comparing with powder diffraction file (PDF) by using the software PDXL.

3-2-4 Nuclear Magnetic Resonance (NMR) measurement

Principle

Nuclear magnetic resonance (NMR) spectroscopy is one of important experimental methods for natural science, such as not only physics and chemistry but also medical science, pharmacy, biological science, material science, and so on. Although NMR is the experimental method utilized by magnetic resonance phenomenon of atomic magnetic momentum, it is widely used for solid state physics whose research subject is mainly electrons, because properties of electrons are reflected in nuclear resonance phenomenon thorough hyperfine interaction between the atom and electron around the atom. Therefore, electronic properties, namely physical properties of materials can be obtained by NMR.

If the nuclear spin nuclear is $\boldsymbol{I}$, and then the nuclear magnetic momentum $\boldsymbol{\mu}$ is represented by,

$$\boldsymbol{\mu} = \gamma \hbar \boldsymbol{I},$$

where γ is the gyromagnetic ratio, and ħ is the Planck constant. Zeeman interaction on the magnetic field $\boldsymbol{H_0}$ which is parallel to z-axis is obtained by,

$$\mathcal{H}_0 = -\boldsymbol{\mu} \cdot \boldsymbol{H_0}$$
$$= -\gamma\hbar \boldsymbol{I} \cdot \boldsymbol{H_0}.$$

Therefore, energy eigenvalue is,

$$E_m = -\gamma\hbar H_0 m,$$

where, m is eigenvalue of I_z which is z-component of $\boldsymbol{I}$, and energy levels are separated with the same gap as shown Fig.3-7.

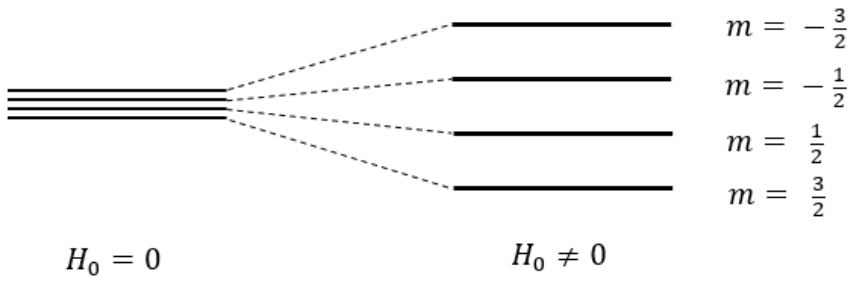

Figure 3-7 Schematic picture of separated energy levels of nuclear spin $\boldsymbol{I}$ (I=3/2) under magnetic field

Thus, degeneracy is resolved by applying static magnetic field H_0 and these separated energy levels are observed by nuclear magnetic resonance absorption. If the static magnetic field H_0 is along to z-axis, and then oscillating magnetic field ($H_1 \cos\omega t$) should be applied perpendicular to z-axis (for example, x-axis) for nuclear magnetic resonance absorption. In this case, the perturbation term is

$$\mathcal{H}_1 = -\gamma\hbar H_1 I_x cos\omega t.$$

This term is added in the Hamiltonian and the resonance condition is

$$\hbar\omega = \gamma\hbar H_0$$

$$\omega = \gamma H_0 \ (= \omega_0),$$

where, the transition between energy level of m and *m*+1 because Ix has matrix element between *m* and *m*+1 and nuclear magnetic resonance phenomenon is observed.

Generally, the resonance frequency is shifted in materials as follows,

$$\omega = \omega_0 + \Delta\omega$$

$$= \gamma(H_0 + H)$$

$$= \gamma H_0(1 - \sigma),$$

where, *H* means the local magnetic field around the nuclear. *H* reflects electron structure around the atom. It is convenient that resonance frequency is represented by chemical shift,

$$\delta = \frac{\omega - \omega^0}{\omega^0} \times 10^6,$$

where ω is the resonance frequency of specific atom and ω^0 is the reference frequency. [3-5-6]

Procedure

NMR was carried to obtain local structure around aluminum tom of Al_2O_3 doped MgH_2 by magic angle spinning (MAS) - NMR spectrometer of JNM-ECA600 (JEOL) at 15 kHz spinning speed. The MAS-NMR spectroscopy was performed at the static magnetic field of 14.1 T and at room temperature. ^{27}Al resonance frequency was 156.4 MHz. Sample powders were packed into 4 mm ZrO_2 rotors under Ar atmosphere. The chemical shift was referenced to 1.0 M $AlCl_3$ aqueous solution as 0 ppm.

3-2-5 X-ray Photoelectron Spectroscopy (XPS) measurement

Principle

The photoelectron spectroscopy is one of spectroscopic experiments that detect intensity of excited photoelectrons from the sample under ultra-high vacuum conditions. The photoelectron can be generated by an electromagnetic wave having constant energy and this phenomenon is called the photoelectric effect. In case of XPS, X-ray was utilized as the electromagnetic wave and core electron within the atom are emitted as photoelectron from the sample irradiated with X-ray. The energy of the photoelectron ε_K is represented by,

$$\varepsilon_K = h\nu - \varepsilon_B,$$

where, h is Planck constant and ε_B is the binding energy of the core electron. Therefore, the binding energy was obtained from the energy of the photoelectron by the XPS with characteristic X-ray. This means that information about the chemical bonding state of the atom or element can be analyzed by the XPS [3-7].

Procedure

XPS was carried out to obtain the binding energy of 2*p*-Aluminum in Al_2O_3 doped MgH_2 after lithium insertion and extraction reaction by ESCALAB-250Xi (Thermo Fisher SCIENTIFIC) with using a focused monochromatized Al Kα radiation of $h\nu$= 1486.6 eV. The XPS spectrometer was directly connected to Ar glove-box with a mobile transfer chamber in order to prevent samples from exposure air or moisture. The spectrometer calibrated with the binding energy of Ag $3d_{5/2}$.The the pressure in the analysis chamber was 5×10^{-7} Pa.

3-2-6 Chronopotentiometry (CP) measurement

Principle

The chronopotentiometry is one of electrochemical techniques, which is based on a controlled current technique. The choronopotentiometry is similar to the choronoamperometry which is based on a controlled potential technique. In this technique, the constant current is applied between the working electrode and the counter electrode, and it provides potential change as a function of time. In addition, the specific capacity (Q) of electro-active materials is obtained by the chronopotentiometry measurement as a following formula,

$$Q = (i \times t)/w,$$

where i is the current density, t is the current applied duration time, and w is weight of the electro-active material. Thus, so-called charge-discharge curve was obtained by the chronopotentiometry. Generally, the potential curve contains a plateaus feature corresponding to the redox potentials of electro-active materials.

The choronopotentiometry is done with a galvanostat apparatus, which is mainly composed of two parts. One is a power supply part which remains a constant current regardless of the electrochemical state of the active material in the experimental cell, and the other is a potential recorder which records potential between the working electrode and the counter electrode as a function of time.

Procedure

The choronopotentiometry carried out to obtain lithium insertion and extraction properties of the samples by galvanostat (HJ-SM8, Hokuto Denko Co.) at a voltage between 0.1V and 2.0V versus Li^+/Li potential with current density of 0.05 mA cm^{-2} at the temperature of 100 °C and current density 0.005 mA cm^{-2} at the temperature of 25 °C.

3-2-7 Cell fabrication

Procedure

The experimental half-cell was fabricated by following way [3-8].

1. The solid electrolyte of $80Li_2S$-$20P_2S_5$, active-material, and acetylene black with the weight ratios of 75:15:10 were put into agate mortar and mixed by hand milling for 15 munities. This mixture is expressed as “composite electrode”
2. The solid electrolyte was put into the specially designed pellet molding as shown in Fig.3-8. After that, $80Li_2S$-$20P_2S_5$ was pressed by up to 20 MPa for three minutes, where the pellet molding is composed of four parts, A, B, C and D as also shown in Fig.3-8.
3. Composite electrode as working electrode was put into the pellet molding after taking part A, and composite electrode and the solid electrolyte were pressed together up to 45 MPa by part A for few minutes.
4. Lithium metal (15 mm diameter, 0.7mm thickness, Honjo Metal Co., Ltd.) as counter electrode and SUS-foil (15mm diameter) were put on $80Li_2S$-$20P_2S_5$ after taking parts C and D, where lithium metal was touched on the solid electrolyte and SUS-foil was touched on the lithium metal.

5. Part C was put on the SUS-foil and pressed together with composite electrode, solid electrolyte, lithium metal, and SUS-foil up to 20MPa for three minutes.
6. The pellet of the half-cell in all solid state as shown Fig.3-9 was removed from pellet molding.
7. The half-cell in all solid state was put into a commercial cell (Toyo System Co.).

The all procedure was done in glove-box to avoid exposure air and moisture. Step 5 is the important step to recognize extraction reaction. In the case of MgH_2, the lithium extraction reaction could not proceed without step 5 (crinping of lithium metal and solid electrolyte).

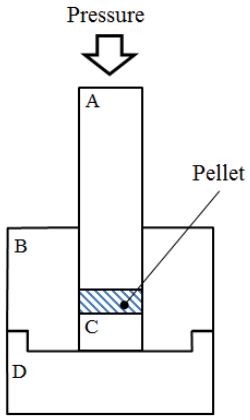

Figure 3-8 Schematic picture of the pellet molding

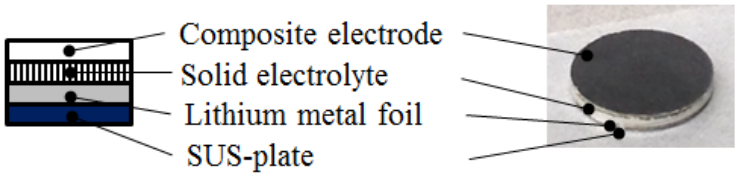

Figure 3-9 Schematic (left) and actual (right) picture of the pellet

References

[3-1] A. Hayashi, S. Hama, H. Morimoto, M. Tatsumisago and T. Minami, *Journal of the American Ceramic Society*, 2001, 84, 477-479.

[3-2] J. Hill, *For Better Thermal Analysis and Calorimetry 3rd ed*., 1991, International Confederation for Thermal Analysis and calorimeter.

[3-3] S. Tanaka and Y. Iida, *Instrumental Analysis*, Shokabo (2000) (Japanese)

[3-4] I. Nakai, X-ray Powder Analysis (Rietveld refinement), ed. I. Nakai and F. Izumi, Asakura Publishing (2002) (Japanese).

[3-5] K. Asayama, *The nuclear magnetic resonance of itinerant electron system*, 2002, Shyoukabou (Japanese)

[3-6] C.P. Slichter, *Principles of Magnetic Resonance (translated by Y.masuda and A.Saika)*, 1998, Spiegel-Verlag Tokyo (Japanese)

[3-7] THE ELECTROCHEMICAL SOCIETY OF JAPAN, THE COMMITTEE OF BATTERY TECHNOLOGY, *Hand book of batteries*, 2010, Ohmsha (Japanese)

[3-8] K. Kanamura, Developments of all solid state secondary batteries, 2007, S&T Publishing inc (Japanese)

4 Results and Discussion

The DTA profile of the composite electrode is shown in Fig 4-1. The composite electrode is the mixture of MgH_2 (active material), $80Li_2S$-$20P_2S_5$ (solid electrolyte), and acetylene black (conductive assistant) by hand milling. Here, the temperature range is from 25 °C to 350 °C and temperature is elevated in 5 °C per minute. Any peak is not observed in the temperature area less than 100 °C, but the peak corresponding exothermic reaction is observed at 232 °C, originated from the solid electrolyte. Actually, according to previous reports, $80Li_2S$-P_2S_5 was transformed from glass ceramic to crystalized state at this temperature [4-1]. This result indicates that any reactions which affect electrical properties of the pristine MgH_2 do not occur at 100 °C. The temperature gives only higher lithium ionic conductivity than that of room temperature.

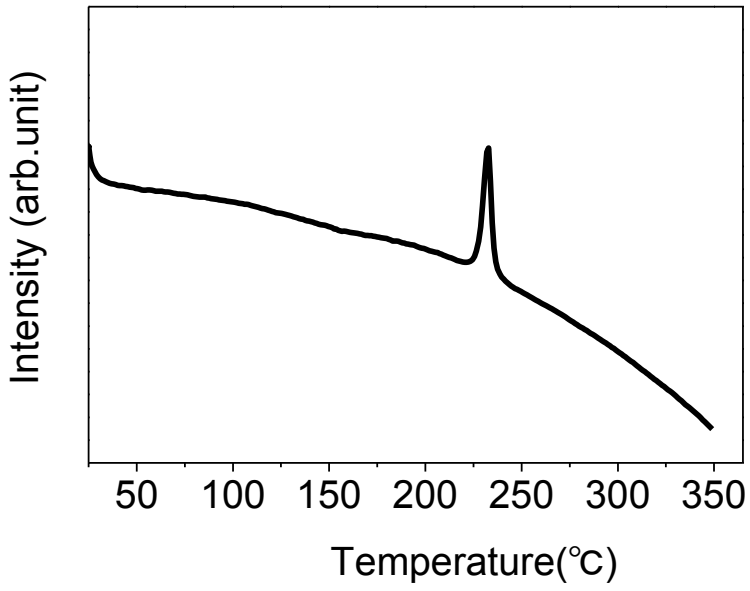

Figure 4-1 DTA profile of the composite electrode containing MgH_2 (active material), $80Li_2S$-$20P_2S_5$ (solid electrolyte), and acetylene black (conductive assistant).

4-1 Anode properties of the pristine MgH_2

4-1-1 Electrochemical properties of the pristine MgH_2

Fig. 4-2 shows the voltage and composition (VC) curve of the pristine MgH_2 for all solid state LIBs. The horizontal axis shows mole fraction of lithium (x) per Mg in the composite electrode. The solid and dotted lines revealed, respectively, Li insertion and extraction reactions of the pristine MgH_2 ($MgH_2 + 2Li^+ + 2e^- \leftrightarrow Mg + 2LiH$) at a current density of 0.05 mA cm^{-2} at 100 °C. Although MgH_2 is not a material for Li insertion-extraction reaction but a material for "conversion" reaction, it is defined that the "Li insertion reaction" is the reaction between MgH_2 and Li, producing Mg and LiH. On the other hand, the "Li extraction reaction" is the reaction between Mg and hydrogen provided from LiH, producing MgH_2 and Li ion.

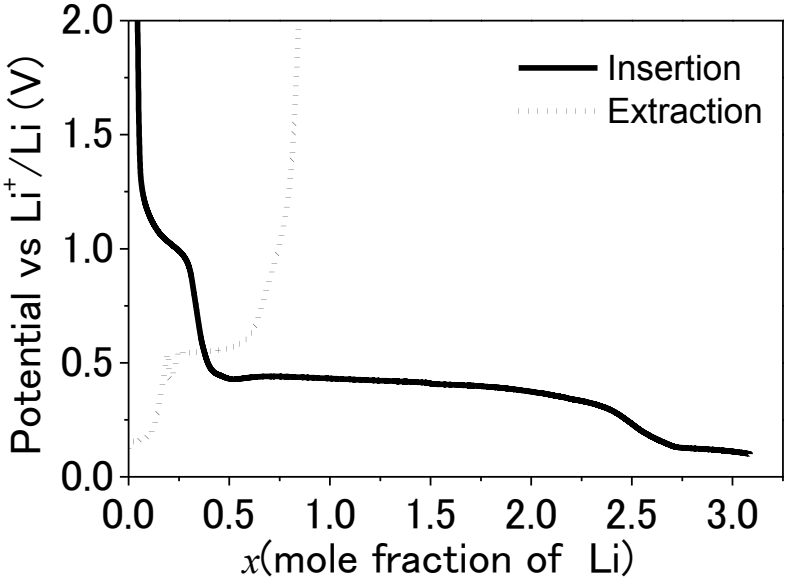

Figure 4-2 VC curve corresponding to Li insertion and extraction reactions of the pristine MgH_2 at a current density of 0.05 mA cm^{-2} and at 100 °C.

Upon the Li insertion reaction, the VC curve shows plateau features located at 1.0V. The plateau located at 1.0V ($0.1 < x < 0.3$) has 0.2 mol g^{-1} of capacity and is not seen above 1.0V on the VC curve upon the Li extraction reaction. Namely this plateau is due to irreversible reaction and not due to reversible reaction of MgH_2 with Li, obviously. Furthermore, the VC curve shows plateau features with a gradual decreasing from 0.45 V ($x = 0.5$) to 0.23V ($x = 2.5$), and then the plateau is observed at 0.1 V ($2.8 < x < 3.1$), which is consistent with the results reported by Oumellal *et al*. [4-2]. In this Li insertion reaction, approximately 3.1 mol g^{-1} Li ions are entered into the composite electrode, forming LiH and a lithium-magnesium alloy. Upon the Li extraction reaction, two plateaus are observed, and the lower and higher plateaus are located at 0.1 V and 0.56 V, respectively. After the voltage reaches 2.0 V, 2.3 mol g^{-1} Li ions still remain in the composite electrode as LiH, indicating that 74% of the entering Li ions in the composite electrode are not able to be extracted. Namely, coulombic efficiency of the pristine MgH_2 is 26%.

4-1-2 XRD profiles of the pristine MgH_2

Fig. 4-3 shows the XRD profiles of the pristine MgH_2 before the Li insertion reaction ($x = 0.0$), after the Li insertion reaction ($x = 3.1$), and after the Li extraction reaction ($x = 0.8$). The peaks corresponding to MgH_2 are observed in the profile of $x = 0.0$, and they disappears after the Li insertion reaction at $x = 3.1$. Lithium-magnesium alloys (Li_3Mg_{17} and Li_3Mg_7) and LiH phases are observed at $x = 3.1$.

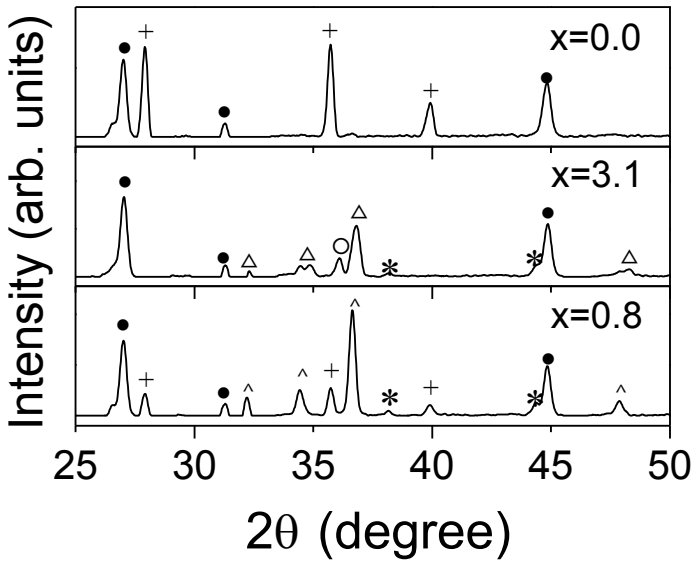

Figure 4-3 XRD profile of the pristine MgH_2 at 100 °C, x = 0.0 (MgH_2, before Li insertion reaction), x = 3.1 (Mg+LiH, after Li insertion reaction), and x = 0.8 (MgH_2, after Li extraction reaction) ●: Solid electrolyte, + : MgH_2, Δ : Li_3Mg_{17}, * : LiH, ^ : Mg, ○ : Li_3Mg_7.

These results suggest that MgH_2 reacts with Li ions electrochemically and transforms into LiH and Mg even in the all solid state LIB as the following as the first step,

$$MgH_2 + 2Li^+ + 2e^- \leftrightarrow Mg + 2LiH \qquad (4\text{-}1),$$

then Mg reacts with Li ions and transforms into a hcp-type lithium-magnesium alloy (Li_3Mg_{17}) as the second step, and afterwards, a bcc-type lithium–magnesium alloy (Li_3Mg_7) is transformed by the further lithium insertion reaction as the third step [4-2-3]. The intensity of the peaks corresponding to MgH_2 increase slightly in the x = 0.8 sample,

indicating that the Li extraction reaction proceeded partially. The peaks corresponding to LiH are observed in the profile at x = 0.8, which is consistent with the fact that 74% of the entering Li ions remain in the composite electrode.

4-2 Anode properties of metal oxides doped MgH_2

Effect of metal oxide additives on anode properties of MgH_2 is discussed in this section, where metal oxides are niobium oxide (Nb_2O_5) and aluminum oxide (Al_2O_3). With respect to the hydrogen absorption (desorption) of MgH_2, it is well known that Nb_2O_5 is the most effective catalyst and Al_2O_3 slightly has catalytic activity [4-4-5].

4-2-1 Anode properties of the Nb_2O_5 doped MgH_2

4-2-1-1 Hydrogen desorption temperatures of the Nb_2O_5 doped MgH_2

The TDMS profiles of hydrogen from the pristine MgH_2 and the (100-y)MgH_2-$y$$Nb_2O_5$ (y=1, 5 mol%) are shown in Fig. 4-4. The hydrogen is desorbed at 410 °C from the pristine MgH_2 and at 272 °C and 346 °C from the 99MgH_2-1Nb_2O_5. The average value of the hydrogen desorption temperatures form the 99MgH_2-1Nb_2O_5 are 309 °C. In addition, The hydrogen is gradually desorbed from the 95MgH_2-5Nb_2O_5 in the temperature range from about 200 °C to 350 °C. Main four peaks (207 °C, 237 °C, 265 °C and 292 °C) are observed on the TDMS profile, and the average value of desorption temperatures are 252 °C) Thus, desorption temperature T_{des} decreases with increasing of Nb_2O_5 contents as follows,

$$T_{des}(MgH_2) > T_{des}(Nb_2O_5;1mol\%) > T_{des}(Nb_2O_5;5mol\%) \quad (4\text{-}2),$$

where, T_{des} (MgH_2), T_{des} (Nb_2O_5;1mol%), T_{des} (Nb_2O_5;5mol%) represent the hydrogen desorption temperature of the pristine MgH_2, the $99MgH_2$-$1Nb_2O_5$, the $95MgH_2$-$5Nb_2O_5$, respectively.

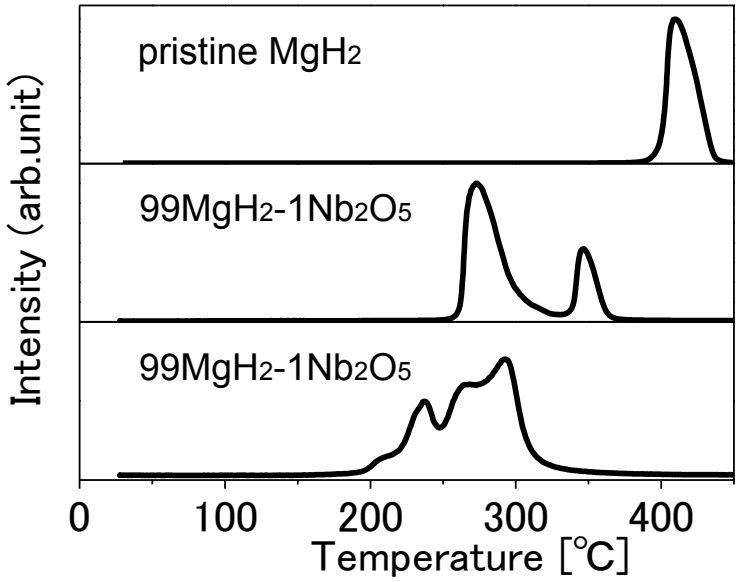

Figure 4-4 TDMS profiles of the pristine MgH_2, the $99MgH_2$-$1Nb_2O_5$ and the $95MgH_2$-$5Nb_2O_5$.

4-2-1-2 Electrochemical properties of the Nb_2O_5 doped MgH_2

The VC curves of the Li insertion reaction corresponding to the pristine MgH_2, the $99MgH_2$-$1Nb_2O_5$ and the $95MgH_2$-$5Nb_2O_5$ are shown in Fig.4-5. In the case of $99MgH_2$-$1Nb_2O_5$, a clear plateau in VC curve located at 0.45 V between x = 0.4 and x = 2.1. After that, the VC curve gradually decreases to the voltage of 0.1 V in the range up to x = 2.7 at a current density of 0.05 mA cm^{-2} at 100 °C. It should be noted that the plateau features became more stable (clearer) for the addition of Nb_2O_5, than that for no additives. In other words, this stabilization of the plateau indicates that the Nb_2O_5

catalyst for the hydrogen desorption kinetics of MgH_2 is also improved the kinetics of the electrochemical reaction to transfer a hydrogen atom from the Mg phase to the Li phase.

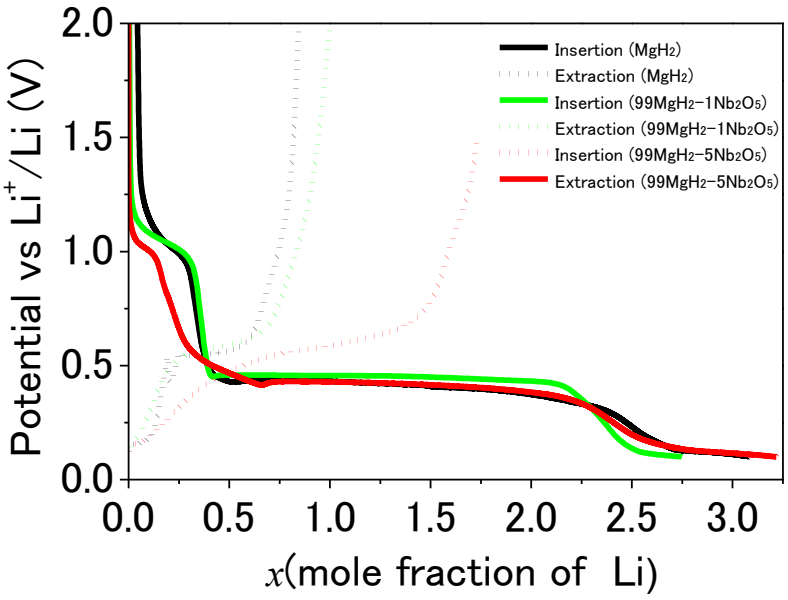

Figure 4-5 VC curves corresponding to Li insertion (solid line) and extraction (dotted line) reactions in the pristine MgH_2 (black line), the $99MgH_2$-$1Nb_2O_5$ (green line) and the $95MgH_2$-$5Nb_2O_5$ (red line) at a current density of 0.05 mA cm^{-2} and at 100 °C

Upon the Li extraction of $99MgH_2$-$1Nb_2O_5$, the VC curve shows plateau features at 0.58 V, but the lower plateau located at 0.1 V, which is seen on the extraction reaction of the pristine MgH_2, is not observed. After the voltage reaches 2.0 V, 1.7 mol g^{-1} Li ions still remain in the composite electrode as LiH, indicating that 63% of the entering Li ions in the composite electrode are not able to be extracted. Namely, coulombic efficiency of $99MgH_2$-$1Nb_2O_5$ is 37%.

The VC curve corresponding to the $95MgH_2$-$5Nb_2O_5$ shows similar curve of the pristine MgH_2 upon the Li insertion. The hydrogen desorbed from the $95MgH_2$-$5Nb_2O_5$

in a lower temperature region than that of the $99MgH_2$-$1Nb_2O_5$ as shown in the TDMS profiles (Fig.4-4). Although hydrogen desorption kinetics of the MgH_2 in the $95MgH_2$-$5Nb_2O_5$ is improved thermodynamically, the kinetics of the electrochemical reaction to transfer a hydrogen atom from the Mg phase to the Li phase seemed not to be improved because the stabilization of the plateau is not observed in the VC curve. Nb_2O_5 is an insulator and exists on the surface of MgH_2, indicating that Nb_2O_5 disturb the physically direct contact between MgH_2 and acetylene black (AB). This situation offers electrical conductive path is obstructed by Nb_2O_5 with increasing contents of Nb_2O_5. This is the reason why the VC curve corresponding to the $95MgH_2$-$5Nb_2O_5$ does not show any stabilization of the plateau. Upon the Li extraction reaction, VC curve of the $95MgH_2$-$5Nb_2O_5$ shows a plateau feature around 0.1 V and 0.6 V. When mole fraction of extracted Li ion is 1.7mol g^{-1} after the voltage reached 1.5 V, the plateau of the $95MgH_2$-$5Nb_2O_5$ has a larger capacity than that of the pristine MgH_2 and the $99MgH_2$-$1Nb_2O_5$. Although the Li extraction of the $95MgH_2$-$5Nb_2O_5$ reaction is measured up to 1.5 V from 0.1 V, the Li extraction reactions of the pristine MgH_2 and the $95MgH_2$-$5Nb_2O_5$ are carried out up to 2.0 V from 0.1V. In order to compare with the results of the pristine MgH_2 and the $95MgH_2$-Nb_2O_5, mole fraction of extracted Li ions reaction of the $95MgH_2$-$5Nb_2O_5$ at 2.0 V is estimated 1.8 mol g^{-1} by linear extrapolation from the value of 1.7 mol g^{-1} at 1.5V. Then, first coulombic efficiency of the $95MgH_2$-$5Nb_2O_5$ at 2.0 V is estimated 56%.

Thus, coulombic efficiency is increased from 26 % (pristine MgH_2) to 37 % ($99MgH_2$-$1Nb_2O_5$) by adding 1 mol% Nb_2O_5. Moreover, the coulombic efficiency is increased from 37 % ($99MgH_2$-$1Nb_2O_5$) to 56% ($95MgH_2$-$5Nb_2O_5$) by adding further

Nb_2O_5. Namely, the coulombic efficiency is increased with increasing Nb_2O_5 contents as follows,

$$Q(MgH_2) < Q(Nb_2O_5;1mol\%) < Q(Nb_2O_5;5mol\%) \quad (4\text{-}3),$$

where, $Q(MgH_2)$, $Q(Nb_2O_5;1mol\%)$, $Q(Nb_2O_5;5mol\%)$ stand for coulombic efficiency of the pristine MgH_2, the $99MgH_2$-$1Nb_2O_5$, the $95MgH_2$-$51Nb_2O_5$, respectively. According to equations of (4-3) and (4-3), it is reasonable to suppose that coulombic efficiency increases with decreasing the hydrogen desorption temperature.

Effect of Nb_2O_5 additive on anode properties of MgH_2 upon the Li extraction reaction is clearer than that upon the lithium insertion reaction. On the reaction formula (4-1), the right hand reaction proceeds easier than left hand because ΔG (MgH_2) is larger than ΔG (LiH). In addition, the reaction which produces Mg from MgH_2 through hydrogen desorption is a transition reaction from insulator of MgH_2 to conductor Mg, so this reaction helps electrochemical reaction of the battery. On the other hand, because proceeding of the left hand reaction is difficult, decreasing of activation energy of hydrogen absorption by adding Nb_2O_5 upon the Li extraction reaction affects the coulombic efficiency to be clearer than decreasing activation energy of hydrogen desorption upon Li extraction reaction.

Fig. 4-6 shows VC curves of the Li insertion reaction corresponding to the pristine MgH_2 (red solid line) and the $99MgH_2$-$1Nb_2O_5$ (blue solid line), respectively at a current density of 0.005 mA cm^{-2} and at 25 °C. Li ions are inserted into the composite electrode at room temperature as shown in Fig. 4-6. The voltage of the pristine MgH_2 suddenly drops to 0.3 V at $x = 0.1$, and then gradually decreases to 0.1 V as plateau-like

features and 1.6 mol g^{-1} of Li ions are inserted into the composite electrode upon the Li insertion reaction. On the other hand, the VC curve of the $99MgH_2$-$1Nb_2O_5$ shows plateau features located at 0.4 V in the range from x = 0.1 to x = 1.0, and then the voltage gradually decreases to 0.1 V up to x = 1.9. Li ionic conductivity at 25 °C is lower than that at 100 °C, therefore, the current density at 25 °C needed to be smaller than that at 100 °C for the Li insertion reaction

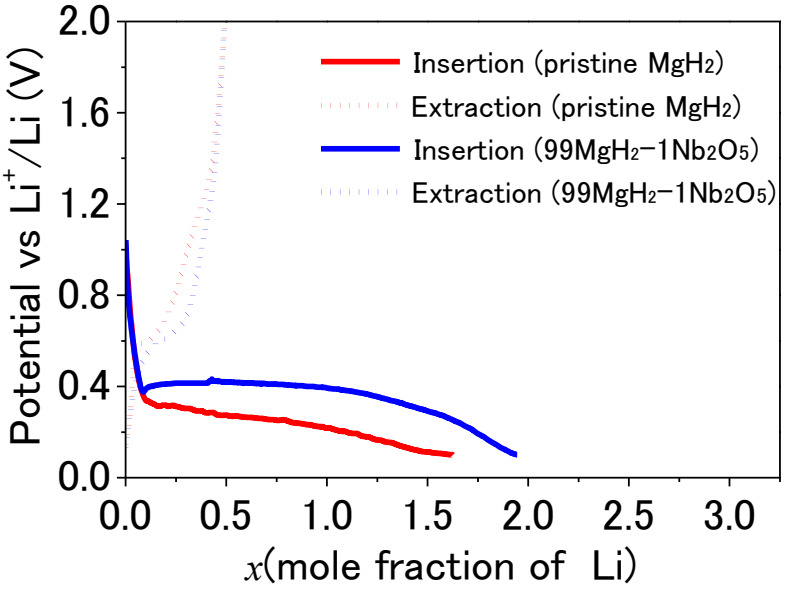

Figure 4-6 VC curves corresponding to Li insertion and extraction reactions of the pristine MgH_2 and the $99MgH_2$-$1Nb_2O_5$ at a current density of 0.005 mA cm^{-2} and at 25 °C.

It should be noted that plateau features became more stable (clearer) for the addition of Nb_2O_5, than that for no additives at 25 °C as well. Moreover, it is clear that the effect of stabilization of the plateau by Nb_2O_5 at 25 °C is more obvious than that at 100 °C. This indicates that the hydrogen transfer process from the Mg phase to Li phase is a rate-determined process at 25 °C. Upon the Li extraction reaction, although both the VC

curves of the pristine MgH_2 (red dotted line) and the $99MgH_2$-$1Nb_2O_5$ (blue dotted line), respectively show plateau features around 0.6 V and Li ions are extracted 0.5 mol g^{-1} after the voltage reaches 2.0 V, the plateau of the $99MgH_2$-$1Nb_2O_5$ had a larger capacity than that of the pristine MgH_2. These properties are consistent with the results at 100 °C.

VC curves corresponding to the Li insertion reaction of the pristine MgH_2 (red line), the $99MgH_2$-$1Nb_2O_5$ (blue line) and the $95MgH_2$-$5Nb_2O_5$ (green line) at a current density of 0.05 mA cm^{-2} (dotted line), 0.15 mA cm^{-2} (solid line) and at 100 °C are shown in Fig. 4-7. Upon the Li insertion reaction, the voltage curve of the pristine MgH_2 shows sudden decrease up to x = 0.5, after that, the voltage curve decreases gradually down to 0.1 V in the range of x = 0.5 to x = 2.0. In the case of the $99MgH_2$-$1Nb_2O_5$, a clear plateau is observed in the voltage located at 0.44 V in the range of x = 0.4 to x = 1.4, after that, the voltage curve decreases down to 0.1 V. In the case of $95MgH_2$-$5Nb_2O_5$, a clear plateau is also observed in the voltage located at 0.4 V in the range of x = 0.4 to x = 1.8, and after that, the voltage curve decrease up to 0.1 V like the voltage curve of the $99MgH_2$-$1Nb_2O_5$. Furthermore, the capacity of the $95MgH_2$-$5Nb_2O_5$ is larger than that of the pristine MgH_2 and the $99MgH_2$-$1Nb_2O_5$. Although the VC curve of the Li insertion reaction corresponding to the $95MgH_2$-$5Nb_2O_5$ shows similar curve of the pristine MgH_2 at current density of 0.05 mA cm^{-2}, the voltage curve of the $95MgH_2$-$5Nb_2O_5$ at current density of 0.15 mA cm^{-2} shows clear plateau and it is quite different from that of the pristine MgH_2. Namely, effect of Nb_2O_5 additives on the anode properties at current density of 0.15 mA cm^{-2} is clearer than that at current density of 0.05 mA cm^{-2}.

Thus, not only coulombic efficiency but also rate properties are improved by adding Nb_2O_5 where the catalysis is well-known as the decrease of the hydrogen desorption temperature. This means that electrochemical properties of coulombic efficiency and rate properties have strong correlation to the improvement of the hydrogen desorption properties in this system.

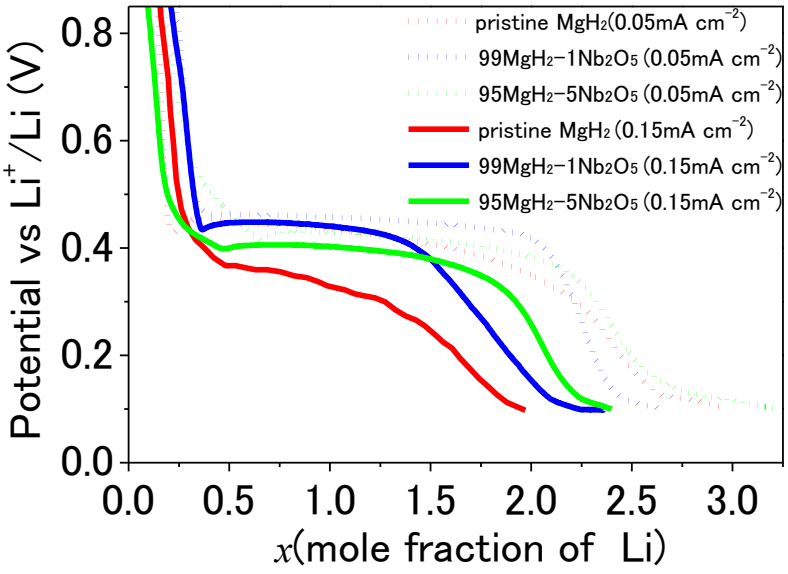

Figure 4-7 VC curves corresponding to the Li insertion reaction of the pristine MgH_2 (red line), the $99MgH_2$-$1Nb_2O_5$ (blue line) and the $95MgH_2$-$5Nb_2O_5$ (green line) at a current density of 0.05 mA cm^{-2} (dotted line), 0.15 mA cm^{-2} (solid line) and at 100 °C

4-2-1-3 XRD profiles of the Nb_2O_5 doped MgH_2

Fig. 4-8 shows the XRD profiles after the Li insertion reaction of three samples, which are the Li inserted $99MgH_2$-$1Nb_2O_5$ at a current density of 0.05 mA cm^{-2} at 100 °C (Fig. 4-8a), the Li inserted $99MgH_2$-$1Nb_2O_5$ at 0.005 mA cm^{-2} and at 25 °C (Fig. 4-8b), and the Li inserted-pristine MgH_2 at a current density of 0.005 mA cm^{-2} and at

25 °C (Fig. 4-8c). The profile of sample (a) reveals that hcp type lithium–magnesium alloy (Li_3Mg_{17}) and LiH are produced. The peaks corresponding to Mg are revealed in the profiles of both the $99MgH_2$-$1Nb_2O_5$ and the pristine MgH_2 after the Li insertion reaction at 25 °C, so it can be said that the Li insertion reaction into MgH_2 phase proceed at 25 °C , namely MgH_2 reacts with Li electrochemically at even room temperature using with a solid electrolyte for LIB. The peaks corresponding to MgH_2 are observed only in the profile of pristine MgH_2 (Fig. 4-8c), indicating that MgH_2 remain in the composite electrode without reacting with Li due to worse reaction kinetics of the pristine MgH_2.

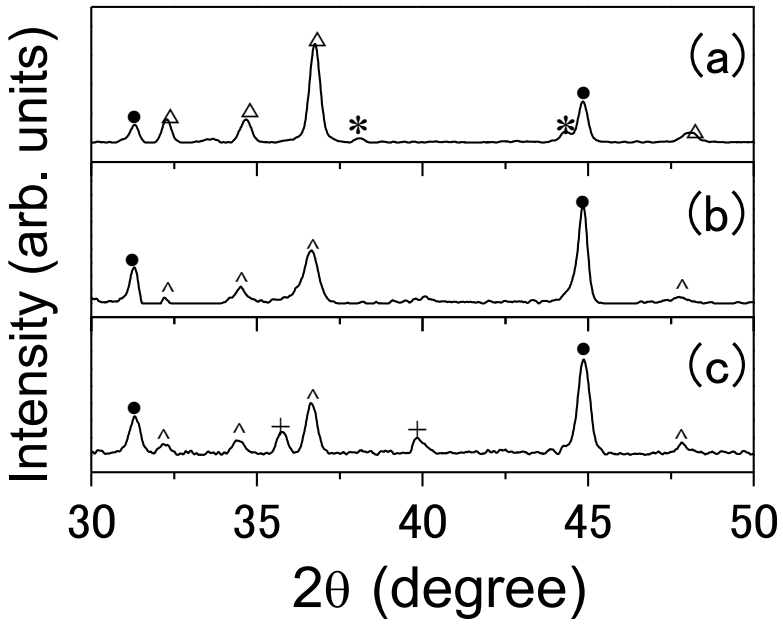

Figure 4-8 XRD profile of the $99MgH_2$-$1Nb_2O_5$ at 100 °C, 0.1V (a), the $99MgH_2$-$1Nb_2O_5$ at 25 °C, 0.1V (b) and the pristine MgH_2 at 25 °C, 0.1V (c) after the Li ion insertion reaction ● : Solid electrolyte, + :MgH_2, △ : $Li_3Mg_{17,}$ * : LiH, ^ : Mg.

4-2-2 Anode properties of the Al_2O_3 doped MgH_2

4-2-2-1 Hydrogen desorption temperatures of the Al_2O_3 doped MgH_2

The TDMS profile of hydrogen from the pristine MgH_2 and the (100-*z*)MgH_2-zAl_2O_3 (z=1, 5, 25 mol%) are shown in Fig. 4-9. The hydrogen desorbed from the 99MgH_2-1Al_2O at 322 °C and 350 °C. The average value of desorption temperatures are 336 °C. The hydrogen is desorbed from the 95MgH_2-5Al_2O_3 at 355 °C. In addition, the hydrogen is desorbed from the 75MgH_2-25Al_2O_3 at 372 °C.

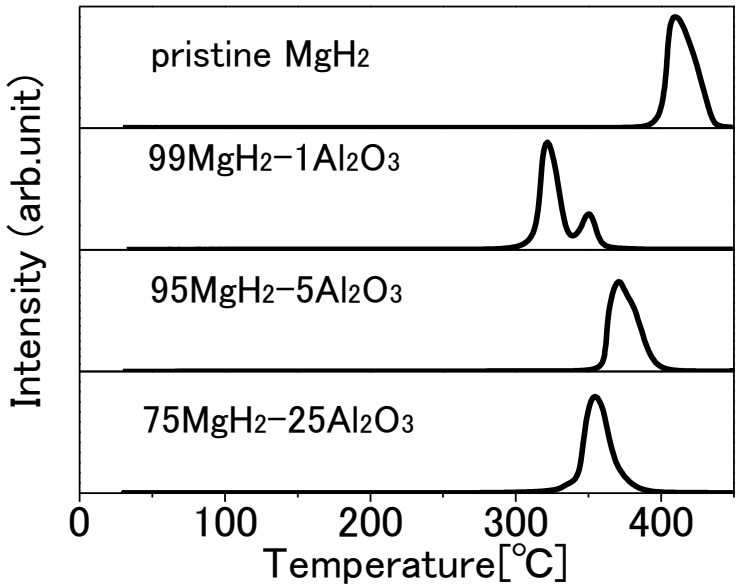

Figure 4-9 TDMS profile of the hydrogen from the pristine MgH_2, the 99MgH_2-1Al_2O_3, the 95MgH_2-5Al_2O_3 and the 75MgH_2-5Al_2O_3.

Thus, although the hydrogen desorption temperature of the (100-*z*)MgH_2-zAl_2O_3 is lower than that of the pristine MgH_2, it seems that the hydrogen desorption temperature from the (100-*z*)MgH_2-zAl_2O_3 is independent on Al_2O_3 contents, as following,

$$T_{des}(MgH_2) > T_{des}(Al_2O_3;1mol\%) \approx T_{des}(Al_2O_3;5mol\%) \approx T_{des}(Al_2O_3;25mol\%) \quad (4\text{-}4),$$

where, T_{des} (MgH_2), T_{des} (Al_2O_3;1mol%), T_{des} (Al_2O_3;5mol%) and T_{des} (Al_2O_3;25mol%) stand for hydrogen desoption temperature of the pristine MgH_2, the $99MgH_2$-$1Al_2O_3$, the $95MgH_2$-$5Al_2O_3$ and the $75MgH_2$-$25Al_2O_3$ respectively.

4-2-2-2 Electrochemical properties of the Al_2O_3 doped MgH_2

VC curves of the pristine MgH_2 and Al_2O_3 doped MgH_2, (1-z) MgH_2-zAl_2O_3 (z = 1, 5, 25 mol%) are shown in Fig.4-10. The solid and dotted lines reveal, respectively, Li insertion and extraction reactions of the pristine MgH_2 (black line) and (1-z) MgH_2-zAl_2O_3 (green, red, and blue lines) at a current density of 0.05 mA cm^{-2} at 100 °C.

Upon the Li insertion reaction, the VC curve of the $99MgH_2$-$1Al_2O_3$ shows a clear plateau in voltage located at 0.45 V between x = 0.4 and x = 2.1. After that, the VC curve gradually decreases to a voltage of 0.1 V in the range up to x = 2.8 at a current density of 0.05 mA cm^2 at 100 °C. This behavior is observed in the VC curve corresponding to the $99MgH_2$-$1Nb_2O_5$. The plateau features became more stable (clearer) by adding Al_2O_3, than that without Al_2O_3. In other words, this stabilization of the plateau indicates that the Al_2O_3 improves the kinetics of the electrochemical reaction to transfer a hydrogen atom from the Mg phase to the Li phase as Nb_2O_5. Although Nb_2O_5 has been well known as the most effective catalyst for hydrogen absorption and desorption into/from MgH_2 according to previous research so far, remarkable difference between the VC curve of the $99MgH_2$-$1Nb_2O_5$ and $99MgH_2$-$1Al_2O_3$ upon the Li insertion reaction are not observed due to low current density of 0.05 mA cm^{-1} and high temperature of 100 °C. It seems that the difference of catalytic ability between Nb_2O_5

and Al_2O_3 become clearer at 25 °C such as Fig. 4-6 or current density of 0.15 mAh cm^{-1} such as Fig. 4-8.

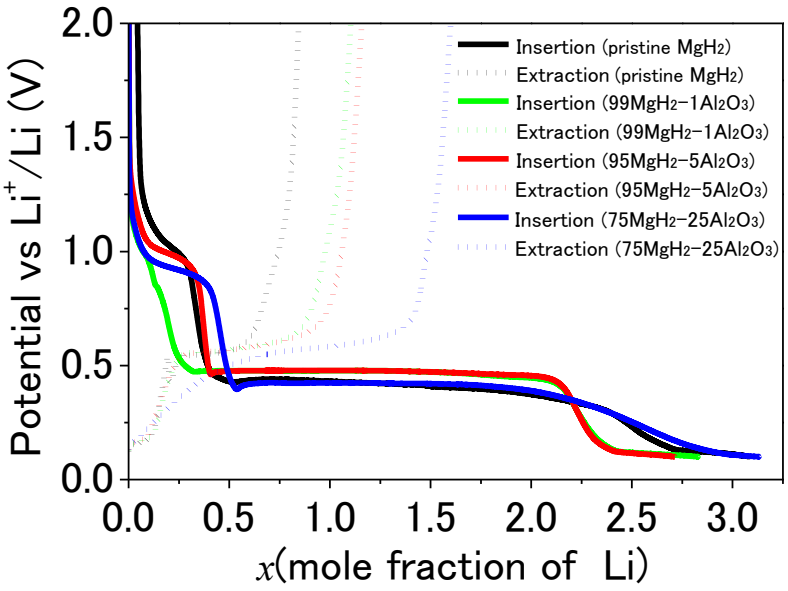

Figure 4-9 VC curves corresponding to Li insertion (solid line) and extraction (dotted line) reactions of the pristine MgH_2 (black line), the $99MgH_2$-$1Al_2O_3$ (green line), the $95MgH_2$-$5Al_2O_3$ (red line) and the $75MgH_2$-$25Al_2O_3$ (blue line) at a current density of 0.05 mA cm^{-2} and at 100 °C.

Upon the Li extraction reaction, the VC curve shows two plateaus. The lower plateau is located at 0.1 V and higher plateau is located at 0.58V which are seen on the extraction reaction of the pristine MgH_2. The VC curve shows gradual increase from 0.54V (x = 0.3) to 0.65V (x = 0.9) at higher plateau After the voltage reaches 2.0 V, 1.7 mol g^{-1} Li ions still remain in the composite electrode as LiH, indicating that 61% of the entering Li ions in the composite electrode are not able to be extracted. Namely, coulombic efficiency of the $99MgH_2$-$1Al_2O_3$ is 39 %. Coulombic efficiency of the pristine MgH_2 is 27%. This means that the coulombic efficiency is increased by adding Al_2O_3.

Upon the Li insertion and extraction reactions, the VC curve of the $99MgH_2$-$5Al_2O_3$ shows the same behavior of $95MgH_2$-$1Al_2O_3$. Upon the Li insertion reaction, 2.7 mol g^{-1} Li ions are inserted. After the voltage reaches 2.0 V, 1.5 mol g^{-1} Li ions still remain in the composite electrode as LiH, indicating that 56% of the entering Li ions in the composite electrode are not able to be extracted. Namely, coulombic efficiency is 44%. This mean that the coulombic efficiency of the $95MgH_2$-$5Al_2O_3$ increases slightly compared with that of the $99MgH_2$-$1Al_2O_3$.

VC curves corresponding to Li insertion and extraction reactions of the $75MgH_2$-$25Al_2O_3$ show similar curves of the pristine MgH_2 and the $95MgH_2$-$5Nb_2O_5$. Upon the Li insertion reaction, the voltage shows plateau features with gradual decrease from 0.45 V (x = 0.5) to 0.23V (x = 2.5), and then the plateau is observed at 0.1 V ($2.8< x < 3.1$). In this Li insertion reaction, approximately 3.1 mol g^{-1} Li ions enter the composite electrode, forming LiH and a lithium-magnesium alloy. The VC curve do not show clear plateau which is seen in the VC curve corresponding to the $99MgH_2$-$1Al_2O_3$ and the $95MgH_2$-$5Al_2O_3$ upon the Li insertion reaction, because physically direct contact between MgH_2 and AB which offers that an electrical conductive path is obstructed by Al_2O_3 with increasing contents of Al_2O_3. This phenomena is also observed in the $(1-y)MgH_2$-yNb_2O_5 system.

Upon the Li extraction reaction, the voltage shows plateau features with gradual increase from 0.1V to 0.65V. After the voltage reaches 2.0 V, 1.5 mol g^{-1} Li ions still remain in the composite electrode as LiH and a lithium-magnesium alloy, indicating that 45% of the entering Li ions in the composite electrode are not able to be extracted. Namely, first coulombic efficiency of $75MgH_2$-$25Al_2O_3$ is 52%.

Thus coulombic efficiency is increased from 26% (pristine MgH_2) to 39 % ($99MgH_2$-$1Al_2O_3$) by adding 1 mol% Al_2O_3. Moreover, the coulombic efficiency is increased from 39 % ($99MgH_2$-$1Al_2O_3$) to 44% ($95MgH_2$-$5Al_2O_3$) or 52% ($75MgH_2$-$25Al_2O_3$) by adding further Al_2O_3. Namely, coulombic efficiency of the $(1-z)MgH_2$-zAl_2O_3 system increases as following with increasing Al_2O_3 contents as the $(1-y)MgH_2$-yNb_2O_5 system.

$$Q(MgH_2) < Q(Al_2O_3;1mol\%) < Q(Al_2O_3;5mol\%) < Q(Al_2O_3;25mol\%) \quad (4\text{-}5),$$

where, $Q(MgH_2)$, $Q(Al_2O_3;1mol\%)$, $Q(Al_2O_3;5mol\%)$, $Q(Al_2O_3;25mol\%)$ stand for coulombic efficiency of pristine MgH_2, $99MgH_2$-$1Al_2O_3$, $99MgH_2$-$1Al_2O_3$, respectively.

The cycle properties of $75MgH_2$-$25Al_2O_3$ and MgH_2 are shown in Fig.4-10. Where, a current density is 0.05 mA cm^{-2} and temperature is 100 °C. The capacity of the pristine MgH_2 decreases suddenly to about 200 mAh g^{-1} after 6 cycles. On the other hand, the $75MgH_2$-$25Al_2O_3$ electrode keeps its capacity of 580 mAh g^{-1} after 9 cycles. Thus, cycle properties are also improved by adding Al_2O_3.

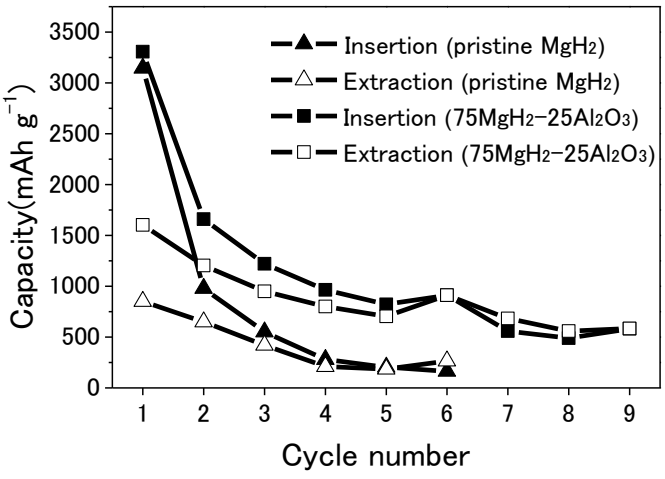

Figure 4-10 Cycle property of $75MgH_2$-$25Al_2O_3$ and MgH_2

Fig. 4-11 shows VC curves corresponding to Li insertion and extraction reactions of the $75MgH_2$-$25Al_2O_3$ at current density of 0.025 mA cm^{-2} at 25 °C. Upon the Li insertion reaction, the voltage (black line) shows a plateau feature with gradual decrease from 0.3 V (x = 0.1) to 0.1V (x = 2.0). It is noteworthy that plateau feature, which is observed on the VC curve corresponding to the Li insertion at 1.0V ($0.1 < x < 0.3$) at 100 °C as shown in Figure 4-9, is not observed at 25 °C. Upon the Li extraction reaction, the voltage (black dotted line) shows plateau feature with a gradual increase from 0.25V to 0.75V. After the voltage reaches 2.0 V, 1.1mol g^{-1} Li ions are extracted. Namely, coulombic efficiency of $75MgH_2$-$25Al_2O_3$ at room temperature is 55%. Although its reversible capacity decreases drastically from 1171 mAh g^{-1} to 906 mAh g^{-1} after five cycles, the reversible capacity decreases gradually after five cycles and the electrode keeps capacity of 861 mAh g^{-1} after ten cycles.

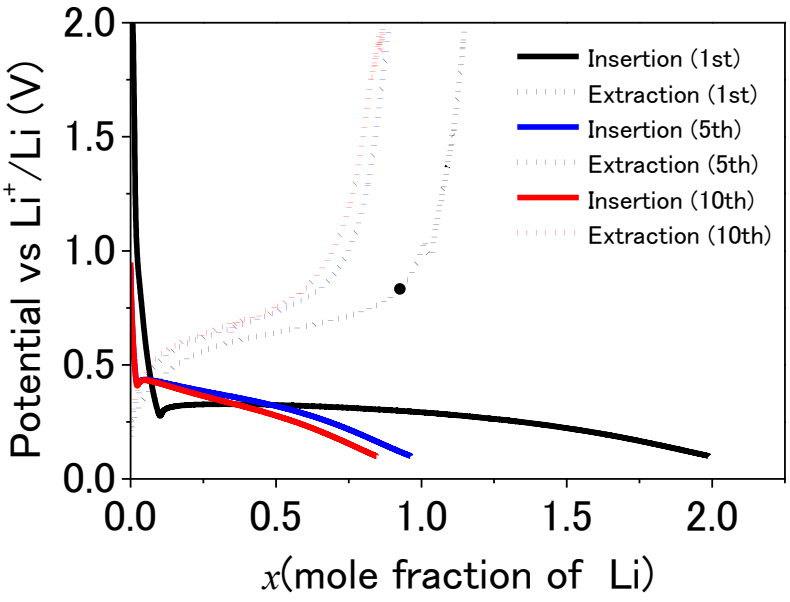

Figure 4-11 VC curves corresponding to Li insertion (solid line) and extraction (dotted line) reactions of the $75MgH_2$-$25Al_2O_3$ (blue line) at a current density of 0.025 mA cm^{-2} at 25 °C

4-2-2-3 XRD profiles of the Al_2O_3 doped MgH_2

Fig. 4-12 shows XRD profiles after the Li insertion reaction of two samples, which are the Li inserted $95MgH_2$-$5Al_2O_3$ at x=2.7 and the Li inserted $75MgH_2$-$25Al_2O_3$ at x=3.1 at a current density of 0.05 mA cm^{-2} at 100 °C. The profile of the $95MgH_2$-$5Al_2O_3$ reveals that hcp type lithium–magnesium alloy (Li_3Mg_{17}) is generated after the Li insertion. The profile of the $75MgH_2$-$25Al_2O_3$ reveals that the hcp type lithium-magnesium alloy (Li_3Mg_{17}) and the bcc type lithium-magnesium alloy (Li_3Mg_7) are generated after the lithium insertion. The hcp type lithium-magnesium alloy and the bcc type lithium-magnesium are also observed in case of the pristine MgH_2 or the (1-y)MgH_2-yNb_2O_5. These results indicate that MgH_2 in the $95MgH_2$-$25Al_2O_3$ and the $75MgH_2$-$25Al_2O_3$ reacts with Li ion and produce Mg and LiH. Furthermore, Mg reacts with Li ion and hcp type lithium-magnesium alloy or bcc type lithium-magnesium alloy are produced in the case of (1-z)MgH_2-zAl_2O_3 as the pristine MgH_2 or the (1-y)MgH_2-yNb_2O_5. Thus, it is difficult to explain why the coulombic efficiency is increased with increasing Al_2O_3 contents by the results of XRD measurements.

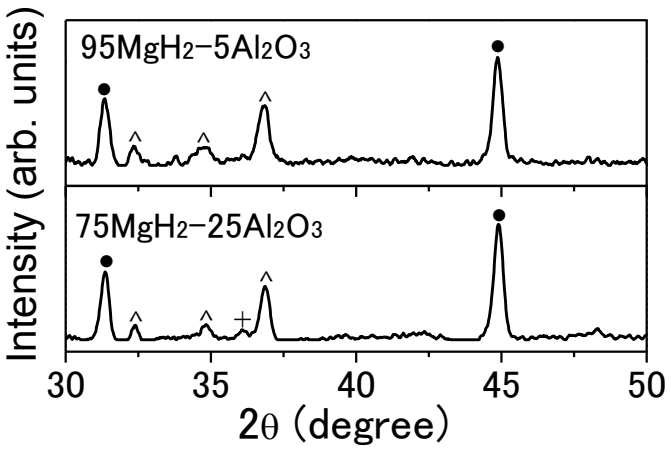

Figure 4-12 XRD profiles of the $95MgH_2$-$5Al_2O_3$ at x=2.75 and the $75MgH_2$-$25Al_2O_3$, at x=3.0. ● : Solid electrolyte, + :Li_3Mg_7, ^ : Li_3Mg_{17}.

4-2-3 Coulombic efficiency of the Nb_2O_5 doped MgH_2 and the Al_2O_3 doped MgH_2

The contents dependence of Nb_2O_5 and Al_2O_3 with respect to the hydrogen desorption temperature corresponding to the (1-y)MgH_2-$y$$Nb_2O_5$ (open square), the (1-z)MgH_2-$z$$Al_2O_3$ (open circle) and the pristine MgH_2 (open triangle) are shown in Fig.4-13. The hydrogen desorption temperature decreases after the addition of both of Nb_2O_5 and Al_2O_3. Although the hydrogen desorption temperature of the (1-y)MgH_2-$y$$Nb_2O_5$ decreases with increasing Nb_2O_5 contents, it seems that the hydrogen desorption temperature of the (1-z)MgH_2-$z$$Al_2O_3$ is independent on Al_2O_3 contents.

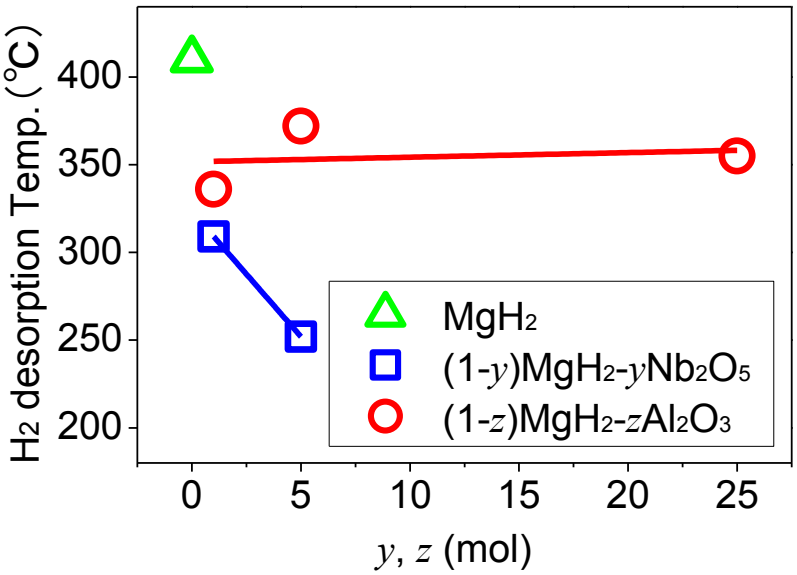

Figure 4-13 Contents dependence of Nb_2O_5 and Al_2O_3 with respect to the hydrogen desorption temperature corresponding to the (1-*y*)MgH_2-*y*Nb_2O_5 (open square), the (1-*z*)MgH_2-*z*Al_2O_3 (open circle) and the pristine MgH_2 (open triangle).

Coulombic efficiency increased with increasing contents of Nb_2O_5 and Al_2O_3 as shown in Fig. 4-14. The coulombic efficiency is increasing with decreasing hydrogen desorption temperature in the (1-*y*)MgH_2-*y*Nb_2O_5. Upon the lithium extraction reaction, the kinetics of the electrochemical reaction and enabled transfer of a hydrogen atoms from LiH to Mg is improved by adding Nb_2O_5. The activation energy of the hydrogen absorption of Mg from LiH is decreased by Nb_2O_5. In addition, the effect to the decreasing of activation energy for the hydrogen absorption becomes clear with increasing Nb_2O_5 contents.

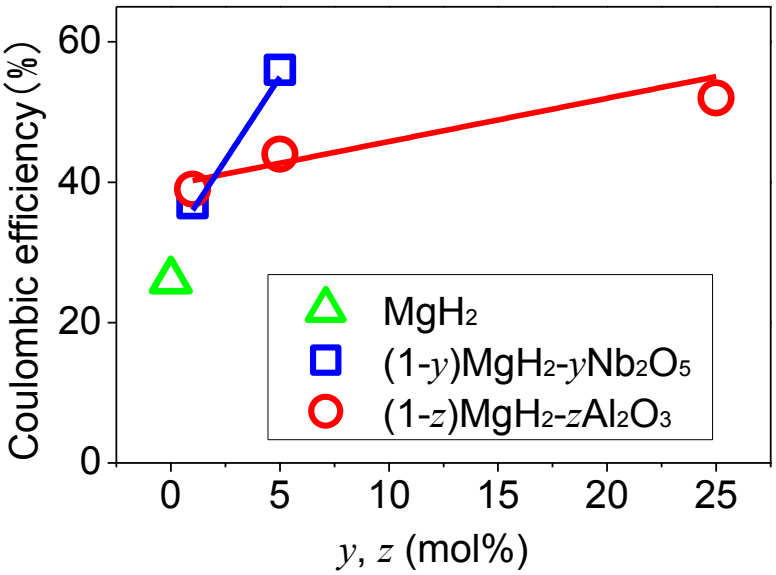

Figure 4-14 Contents dependence of Nb_2O_5 and Al_2O_3 with respect to the coulombic efficiency of the (1-*y*)MgH_2-*y*Nb_2O_5 (open square), the (1-*z*)MgH_2-*z*Al_2O_3 (open circle) and the pristine MgH_2 (open circle).

Thus, there is an extremely strong correlation between hydrogen ab/desorption properties and anode properties, in particular the coulombic efficiency, of the (1-*y*)MgH_2-*y*Nb_2O_5,. On the other hand, it seems that there is slight correlation between hydrogen ab/desorption properties and the coulombic efficiency of the (1-*z*)MgH_2-*z*Al_2O_3 .

Although the coulombic efficiency is increased with increasing Al_2O_3 contents, the hydrogen desorption temperature is independent on Al_2O_3 contents. This indicates that there exists different mechanism on the increasing of the coulombic efficiency from decreasing of the activation energy with respect to the hydrogen ab/desorption by adding Al_2O_3.

Summary

Reversible Li insertion and extraction reactions of the pristine MgH_2 for all solid-state LIBs are investigated at current density of 0.05 mA cm^{-2} at 100 °C. Upon the Li insertion reaction, 3.0 mol g^{-1} Li ions are inserted into the pristine MgH_2 as electrode. Upon the Li extraction reaction, only 0.8 mol g^{-1} Li ions are extracted from electrode. Namely, coulombic efficiency of the pristine MgH_2 was 28%. The XRD profiles of the pristine MgH_2 upon the Li insertion reaction suggested that MgH_2 reacts with Li ions electrochemically, producing Mg and LiH even in the all solid state LIBs as the first step, then Mg reacts with Li ions and transforms into a hcp-type lithium-magnesium alloy (Li_3Mg_{17}) as the second step, and afterwards a bcc-type lithium–magnesium alloy (Li_3Mg_7) is produced as the third step upon the Li insertion reaction. On the other hand, the peaks corresponding to Mg and LiH are observed after the Li extracted reaction, indicating that the entering Li ions remain in the pristine MgH_2 as electrode. This result is consistent that the pristine MgH_2 shows low coulombic efficiency.

Effects of Nb_2O_5 additives on anode properties of MgH_2 for all solid state LIBs are investigated at current density of 0.05 mA cm^{-2} and 0.15 mA cm^{-2} at 100 °C and the following results are revealed. (1) The hydrogen desorption temperature decreases with increasing Nb_2O_5 contents and columbic efficiency increases with increasing Nb_2O_5 contents. Therefore, there is an extremely strong correlation between hydrogen ab/desorption properties and anode properties, in particular the coulombic efficiency of MgH_2. (2) Rate properties of MgH_2 are also improved with increasing Nb_2O_5 contents. (3) Effect of Nb_2O_5 additives on anode properties of MgH_2 is clearer upon the Li extraction reaction than that upon the Li insertion reaction due to thermodynamically and electrochemically reasons. (4) Upon the Li insertion reaction, effect of Nb_2O_5 additives

become clearer at current density of 0.15 mA cm^{-2} than that of 0.05 mA cm^{-2}. In addition, Nb_2O_5, is able to stabilize the plateau on the VC curve upon the Li insertion reaction at 25 °C as well. Moreover, it is clear that the effect of stabilization of the plateau by Nb_2O_5 at 25 °C is more obvious than that at 100 °C. This indicates that the hydrogen transfer process from Mg phase to Li phase is a rate-determined process at 25 °C.

Effects of Al_2O_3 additives on anode properties of MgH_2 for all solid state LIBs are investigated at current density of 0.05 mA cm^{-2} at 100 °C and the following results were revealed, (1) Culombic efficiency is increased with increasing Al_2O_3 contents. On the other hands, the hydrogen desorption temperature is independent on Al_2O_3 contents. Therefore, it seems that there is slight correlation between hydrogen ab/desorption properties of the Al_2O_3 doped MgH_2 and its coulombic efficiency. This indicates that there exists different mechanism on the increasing of the coulombic efficiency from decreasing of the activation energy with respect to the hydrogen absorption and desorption by adding Al_2O_3. (2) Cycle properties is also inproved by adding Al_2O_3. For example, $75MgH_2$-$25Al_2O_3$ keeps its capacity of 580 mAh g^{-1} after 9 cycles a current density of 0.05 mA cm^{-2} at 100 °C. Moreover, $75MgH_2$-$25Al_2O_3$ shows excellent cycle properties at room temperature and has capacity of 861 mAh g^{-1} after ten cycles.

4-3 Mechanisms on the increasing of the coulombic efficiency of the Al_2O_3 doped MgH_2

XPS and ^{27}Al MAS-NMR measurements are carried out to clarify mechanism on the increasing of the coulombic efficiency with increasing Al_2O_3 contents.

4-3-1 XPS profiles of the Al_2O_3 doped MgH_2

Fig.4-15 shows results of XPS measurements of the $95MgH_2$-$5Al_2O_3$ and the $75MgH_2$-$25Al_2O_3$ after ball milling for 20h.

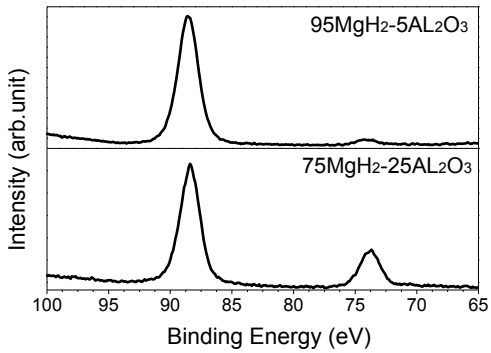

Figure 4-15 XPS Al 2p and Mg 2s peaks of $95MgH_2$-$5Al_2O_3$ and $75MgH_2$-$25Al_2O_3$ after ball milling for 20 hours before Li insertion reaction.

In the case of the $95MgH_2$-$5Al_2O_3$, there are two peaks corresponding to Mg 2s at 88.6eV and Al 2p at 74.2eV. In the case of the $75MgH_2$-$25Al_2O_3$, two peaks corresponding to Mg 2s at 88.4ev and Al 2p at 73.8 eV are also observed. According to a literature, Al 2p of pristine Al_2O_3 peak is observed at 74.4 eV [4-6]. Therefore, Al takes the same chemical state as Al_2O_3 in the $95MgH_2$-$5Al_2O_3$ and the $75MgH_2$-$25Al_2O_3$. Namely, Al is not changed its chemical state by ball milling. Although the coulombic efficiency of the $95MgH_2$-$5Al_2O_3$ is quite different from of the $75MgH_2$-$25Al_2O_3$, chemical state of Al is the same in starting materials of them.

4-3-2 NMR profiles of Al_2O_3 doped MgH_2

There are many alumina polymorphs, and many researchers have studied and revealed their structures on an atomic scale by ^{27}Al MAS-NMR [4-7-12]. It has been

well known that there are three types of coordination of the Al^{3+}, which are tetrahedral coordination (AlO_4), pentahedral coordination (AlO_5) and octahedral coordination (AlO_6) in alumina polymorphs and its precursors as shown in table 4-1 [4-13].

Table 4-1 Weight ratio of AlO_4, AlO_5 and AlO_6 in alumina polymorphs and precursors [4-13]

	AlO_4 (%)	AlO_5 (%)	AlO_6 (%)
Gibbsite	100	0	0
Boehmite	100	0	0
ρ-Al_2O_3	55	25	20
ε-Al_2O_3	71±1	21±1	0
χ-Al_2O_3	73	20	7
κ-Al_2O_3	75	25	0
γ-Al_2O_3	72±4	29.5±4	1.5±4
ε'-Al_2O_3	69	31	0
δ-Al_2O_3	57	43	0
θ-Al_2O_3	57.5±4.5	42.5±4.5	0
α-Al_2O_3	100	0	0

In particular, γ-Al_2O_3 has been applied practically as support material for metal catalysis. Kwak *et al*. reported that pentahedral coordinated (coordinatively unsaturated) Al^{3+} on the γ-Al_2O_3 surfaces acted as binding site for such as PtO, which is the precursor for metallic Pt and utilized widely [4-14]. Namely, the pentahedral coordinated Al^{3+} is the origin of the so called strong metal-support interaction. They observed decreasing the intensity of the pentahedral coordinated Al^{3+} atom and increasing the intensity of the octahedral coordinated Al^{3+} by ^{27}Al MAS-NMR during loading Pt onto γ-Al_2O_3 at 573K. They insisted that these results suggested that Pt atom bind to the pentahedral coordinated Al^{3+} cite. Therefore, it seems that the synthesis of γ-Al_2O_3 is quite important,

which possesses pentahedral coordinated Al^{3+} in terms of application of Al_2O_3 as support material for active catalyst.

Although it has been known that pentahedral coordinated Al^{3+} induced thermally during transformation from γ-Al_2O_3 phase to α-Al_2O_3 phase by thermal treatment, Düvel *et al*. reported that pentahedral coordinated Al^{3+} was also generated by ball milling during phase transformation from γ-Al_2O_3 phase to α-Al_2O_3. They investigated the process of the transformation from γ-Al_2O_3 phase to α-Al_2O_3 phase by ^{27}Al MAS-NMR [4-15]. Moreover, they also reported the phase transformation was inhibited by adding a certain amount of CaF_2 because pentahedral coordinated Al^{3+} was coordinated immediately by CaF_2.

Since pentahedral coordinated Al^{3+} is coordinated by CaF_2 or PtO during ball milling or heat treatment, it seemed to say that the pentahedral coordinated Al^{3+} sites act as binding site against CaF_2 or PtO.

Fig.4-16 shows ^{27}Al MAS-NMR spectra of the pristine Al_2O_3 (Fig.4-16(a)) and the 20h milled Al_2O_3 (Fig.4-16(b)). There are two peaks corresponding to AlO_4 at 66.0 ppm and AlO_6 at 10.6 ppm in the pristine Al_2O_3 as shown in Fig 4-16(a). The weight ratio of AlO_4 and AlO_6 in the pristine Al_2O_3 are 33.6 % and 66.4%, respectively. Therefore, the pristine Al_2O_3 is consistent with γ-Al_2O_3 or γ'-Al_2O_3 according to table 4-1. On the other hand, there are three peeks corresponding to AlO_4 at 63.9 ppm, AlO_5 at 33.4 ppm and AlO_6 at 14.2 ppm in the 20h milled Al_2O_3 as shown in Fig 4-16(b). AlO_6 is shifted from at 10.6 ppm to 14.2 ppm by ball milling 20h. This means that the transformation from γ-Al_2O_3 phase to α-Al_2O_3 is induced by ball milling for 20h. In addition, pentahedral coordinated Al^{3+} is generated during ball milling.

^{27}Al MAS-NMR measurement is carried out to obtain information of the local coordination of the Al^{3+} in (100-*z*) MgH_2-*z*Al_2O_3 (*z*=1, 5, 25 mol %) system.

^{27}Al MAS-NMR spectra of 99MgH_2-1Al_2O_3 are shown in Fig.4-16. Table 4-2 shows the weight ratio of AlO_4, AlO_5 and AlO_6 in 99MgH_2-1Al_2O_3. The weight ratio was obtained by rough fitting-curve which is composed of Gaussian and Lorentzian function. Fig.4-16 (a) shows the ^{27}Al MAS-NMR spectra of 99MgH_2-1Al_2O_3 before lithium insertion reaction, in other words, after loading Al_2O_3 to MgH_2 by ball milling 20h. There are also two peaks at 10.1 ppm and 64.5 ppm corresponding to AlO_4 and AlO_6 as in the case of pristine Al_2O_3. Phase transformation of the Al_2O_3 and generation of pentahedral coordinate aluminum atom are inhibited by MgH_2. It seems that MgH_2 immediately coordinated to the pentahedral-coordinated aluminum atom and prevent the phase transformation as CaF_2. This result is consistent with the results of Düvel *et al*. After the lithium insertion reaction (Fig.4-16 (b), the weight ratio of AlO_4 decreases from 36.9% to 7.7% and the peak corresponding to AlO_6 shifts from 10.1 ppm to 14.4 ppm and its peak intensity increases from 63.1% to 73.6%. In addition, AlO_5 is observed at 33.2 ppm. As mentioned above, the peek shift of AlO_6, the decreasing of the weight ratio of AlO_4 and the generation of the AlO_5 were also observed thermal and mechanical phase transformation from γ-Al_2O_3 phase to α-Al_2O_3 phase. Therefore, the phase transformation is induced during lithium insertion reaction of the 99MgH_2-1Al_2O_3. In addition, MgH_2 reacts with lithium ion and produces Mg and LiH by its lithium insertion reaction. This is also one of reasons why the new peek corresponding to AlO_5 shows up at 33.2ppm after lithium insertion reaction because unsaturated Al^{3+} is coordinated not by Mg but by MgH_2. It is noteworthy that

unsaturated Al^{3+} is appeared after lithium insertion reaction. This unsaturated Al^{3+} can be also binding cite of LiH as MgH_2, CaF_2 or PtO.

^{27}Al MAS NMR spectra of $95MgH_2$-$5Al_2O_3$ are shown in Fig.4-17. Table 4-3 shows the weight ratio of AlO_4, AlO_5 and AlO_6 in $95MgH_2$-$5Al_2O_3$. The weight ratio is obtained by rough fitting-curve which is composed of Gaussian and Lorentzian function. Before lithium insertion reaction, there are two peaks at 10.5 ppm and 64.6 ppm corresponding AlO_4 and AlO_6 as shown in Fig.4-17 (a). These peaks are observed in pristine Al_2O_3 as shown in Fig.4-17 (d). This means that phase transformation of the Al_2O_3 and generation of pentahedral coordinate aluminum atom are inhibited by MgH_2 as in the case of $99MgH_2$-$1Al_2O_3$. After the Li insertion reaction at x=2.75, the peak intensity corresponding to AlO_4 decreases from 33.6% to 5.5% and the peak corresponding to AlO_6 shifts from 10.5 ppm to 14.2 ppm. In addition, the new peak corresponding to AlO_5 is observed at 33.3 ppm as shown in Fig.4-16 (b). After the Li extraction reaction at x=1.1, three peeks are also observed corresponding to AlO_4 at 63.9 ppm, AlO_5 at 33.4 ppm, and AlO_6 at 14.2 ppm. No phase transformation of Al_2O_3 is observed during lithium extraction reaction.

^{27}Al MAS NMR spectra of $75MgH_2$-$25Al_2O_3$ are shown in Fig.4-18. Table 4-2 shows the weight ratio of AlO_4, AlO_5 and AlO_6 in $75MgH_2$-$5Al_2O_3$. The weight ratio is obtained by rough fitting-curve which is composed of Gaussian and Lorentzian function. Before lithium insertion reaction, there are two peaks at 9.5 ppm and 63.6 ppm corresponding AlO_4 and AlO_6 as shown in Fig.4-17(a). Although the peak intensities of AlO_4 and AlO_6 in $75MgH_2$-$25Al_2O_3$ are different from that in pristine Al_2O_3, the peak positions of AlO_4 and AlO_6 in $75MgH_2$-$25Al_2O_3$ are the same as that in pristine Al_2O_3 as shown in table 4-4. After the Li insertion at x=3.00, the peak intensity corresponding to

AlO_4 decreases 45% to 20% and the peak position corresponding to AlO_6 shifts from 11.3 ppm to 14.5 ppm and the peak shift corresponding to AlO_6 increases from 55% to 66.9%. In addition, the new peak corresponding to AlO_5 is also observed at 33.4 ppm as shown in Fig.4-17 (b). After the Li extraction reaction at x=1.6, three peeks are also observed corresponding to AlO_4 at 65.5 ppm, AlO_5 at 33.6 ppm, and AlO_6 at 14.2 ppm. Therefore, the local environment of Al atom at x=1.6 does not change from x=3.0. After 9 cycles, these three peaks are also observed. No phase transformation of Al_2O_3 is observed during lithium extraction reaction.

Thus, unsaturated Al^{3+} is observed in (100-z)MgH_2-zAl_2O_3 (z=1, 5, 25 mol%) system. It is natural that unsaturated Al^{3+} can be the binding cite of LiH like PtO, in other words, LiH can be trapped at the surface of MgH_2. If pentahedral coordinated Al^{3+} on the surface of Mg can be so colled binding site, hydrogen path between LiH and Mg is remained, indicating that more Li ions can be extracted from composite electrode. As a result, coulombic efficiency is increased by adding Al_2O_3 because this so called binding cites increases with increasing Al_2O_3 contents. The cycle properties are also improved by adding Al_2O_3 because hydrogen path between LiH and Mg is remained by unsaturated Al^{3+} during lithium insertion and extraction reaction.

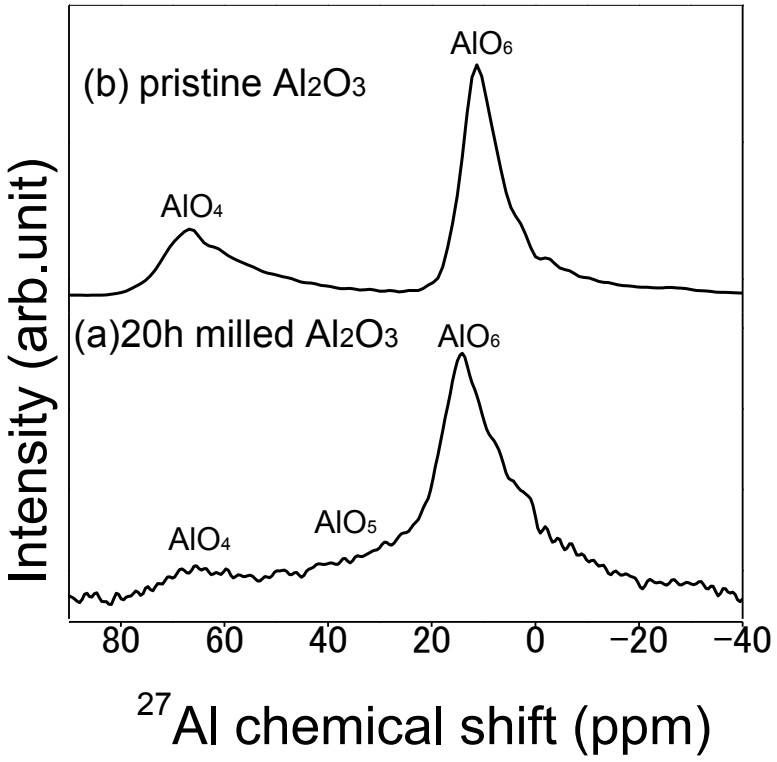

Figure 4-16 ^{27}Al MAS NMR spectra of the pristine Al_2O_3 and the 20h milled Al_2O_3 .

Table 4-2 Weight ratio of AlO_4, AlO_5 and AlO_6 in $99MgH_2$-$1Al_2O_3$ (The value in the parenthesis represents a peak position of chemical shit)

		AlO_4	AlO_5	AlO_6
(a)	x = 0.0	36.9% (64.5ppm)	-	63.1% (10.1ppm)
(b)	x = 2.8	7.7% (63.9ppm)	18.6% (33.2ppm)	73.6% (14.4ppm)
(c)	pristine Al_2O_3	33.6% (66.0ppm)	-	66.4% (10.6ppm)

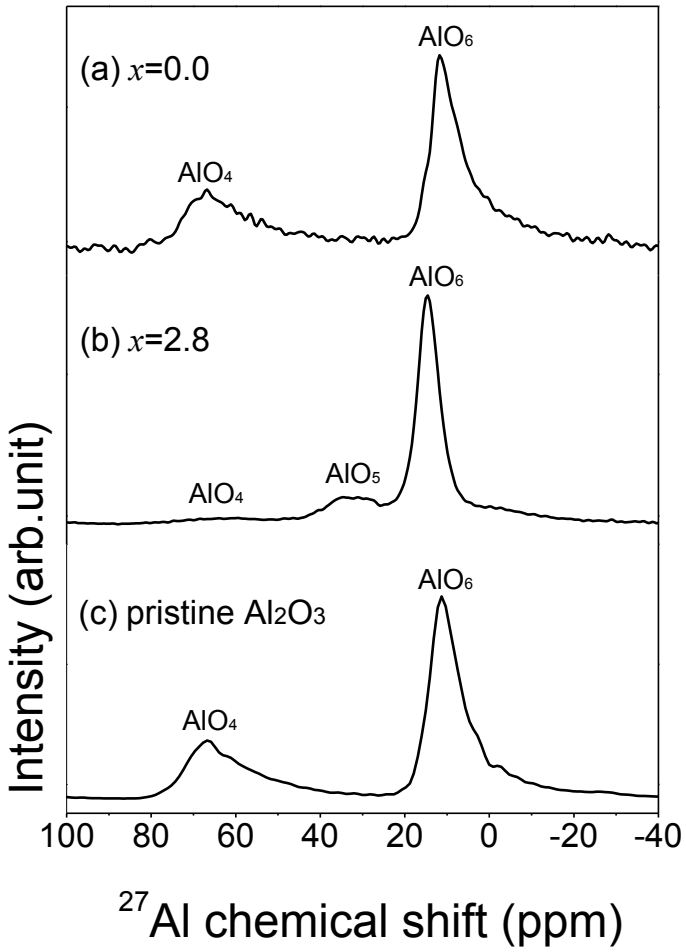

Figure 4-17 ^{27}Al MAS NMR spectra of $99MgH_2$-$1Al_2O_3$.

Table 4-3 Weight ratio of AlO_4, AlO_5 and AlO_6 in $95MgH_2$-$5Al_2O_3$ (The value in the parenthesis represents a peak position of chemical shit)

		AlO_4	AlO_5	AlO_6
(a)	x = 0.0	33.6% (64.6ppm)	-	66.4% (10.5ppm)
(b)	x = 2.7	5.3% (63.8ppm)	19.8% (33.8ppm)	74.8% (14.2ppm)
(c)	x = 1.2	5.5% (63.9ppm)	16.6% (33.4ppm)	77.9% (14.2ppm)
(d)	pristine Al_2O_3	33.6% (66.0ppm)	-	66.4% (10.6ppm)

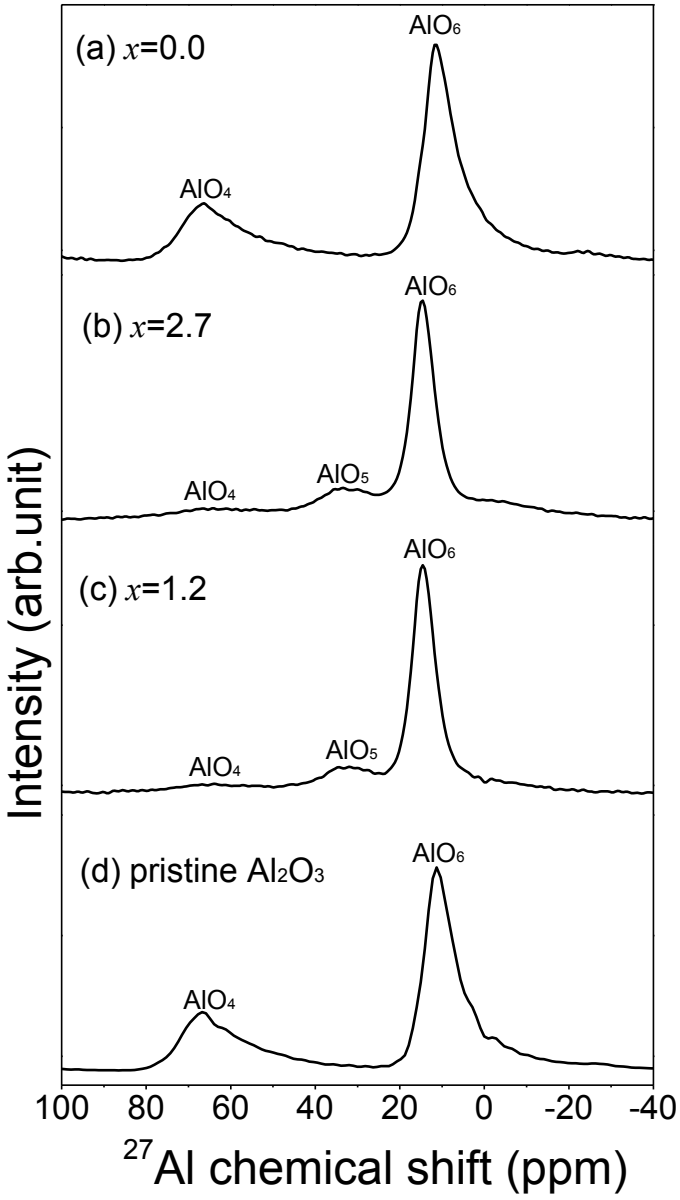

Figure 4-18 ^{27}Al-MAS-NMR spectra $95MgH_2$-$5Al_2O_3$.

Table 4-4 Weight ratio of AlO_4, AlO_5 and AlO_6 in $75MgH_2$-$25Al_2O_3$ (The value in the parenthesis represents a peak position of chemical shit)

	AlO_4	AlO_5	AlO_6
(a) x = 0	45% (63.6ppm)	-	55% (9.5ppm)
(b) x = 3.1	20.0% (64.8ppm)	13.1% (33.5ppm)	66.9% (14.0ppm)
(c) x = 1.6	19.2% (65.5ppm)	14.5% (33.6ppm)	66.3% (14.2ppm)
(d) pristine Al_2O_3	33.6% (66.0ppm)	-	66.4% (10.6ppm)

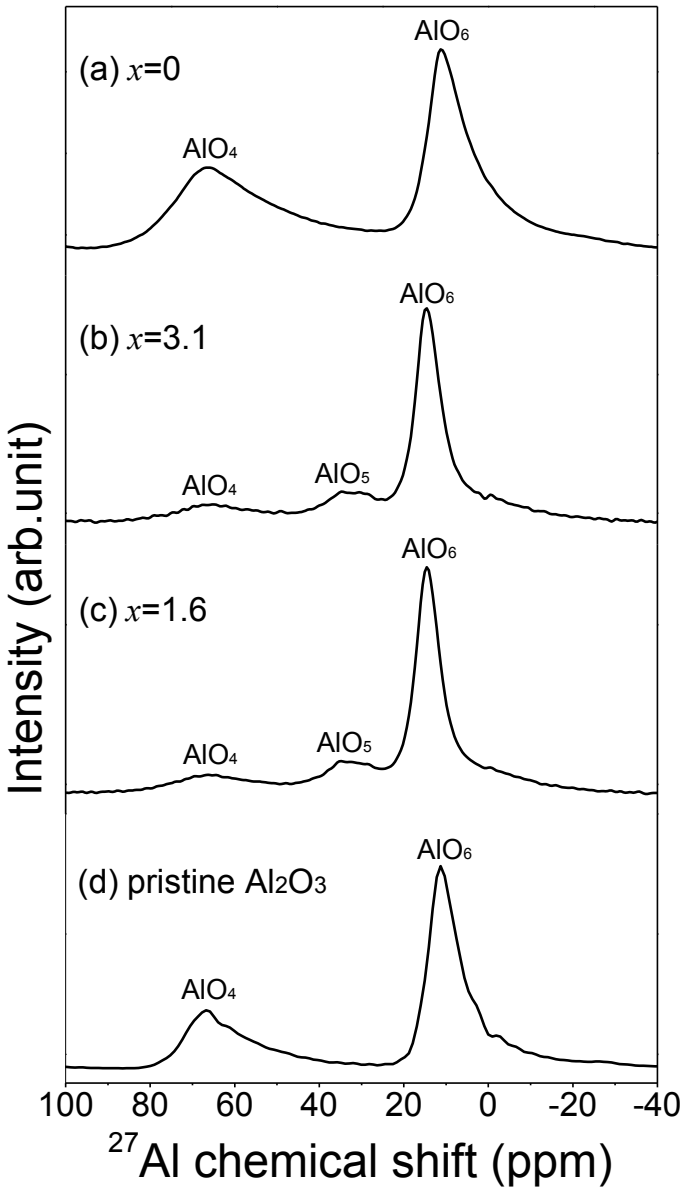

Figure 4-19 ^{27}Al MAS NMR spectra of $75MgH_2$-$25Al_2O_3$.

Summary

^{7}Al MAS-NMR spectra of the pristine Al_2O_3 (Fig.4-16(a)) and the 20h milled Al_2O_3. The transformation from γ-Al_2O_3 phase to α-Al_2O_3 is induced by ball milling for 20h. In addition, pentahedral coordinated Al^{3+} is generated during ball milling.

^{27}Al MAS-NMR measurement is carried out to obtain information of the local coordination of the Al^{3+} in (100-*z*) MgH_2-*z*Al_2O_3 (z=1, 5, 25 mol %) system. Phase transformation of the Al_2O_3 and generation of pentahedral coordinate aluminum atom are inhibited by MgH_2 in (100-*z*) MgH_2-*z*Al_2O_3 (*z*=1, 5, 25 mol %) system. It is seemed that MgH_2 immediately coordinated to the pentahedral-coordinated aluminum atom and prevent the phase transformation. It is noteworthy that unsaturated Al^{3+} is appeared after lithium insertion reaction. This unsaturated Al^{3+} can be also binding cite of LiH. If pentahedral coordinated Al^{3+} on the surface of Mg can be so colled binding site, hydrogen path between LiH and Mg is remained indicating that more Li ions can be extracted from composite electrode. As the result, coulombic efficiency is increased by adding Al_2O_3 because the binding cites increase with increasing Al_2O_3 contents. The cycle property is also improved by adding Al_2O_3 because hydrogen path between LiH and Mg is remained by unsaturated Al^{3+} during lithium insertion and extraction reaction.

References

[4-1] A. Hayashi, S. Hama, T. Minami and M. Tatsumisago, *Electrochemistry Communications*, 2003, 5, 111-114.

[4-2] Y. Oumellal, A. Rougier, G. A. Nazri, J. M. Tarascon and L. Aymard, *Nature Materials*, 2008, **7**, 916-921.

[4-3] S. Brutti, G. Mulas, E. Piciollo, S. Panero and P. Reale, *Journal of Materials Chemistry*, 2012, **22**, 14531-14537.

[4-4] G. Barkhordarian, T. Klassen and R. Bormann, *Scripta Materialia*, 2003, **49**, 213-217.

[4-5] G. Barkhordarian, T. Klassen and R. Bormann, *Journal of Alloys and Compounds*, 2004, **364**, 242-246.

[4-6] S. Verdier, L. El Ouatani, R. Dedryvère, F. Bonhomme, P. Biensan and D. Gonbeau, *Journal of The Electrochemical Society*, 2007, **154**, A1088-A1099.

[4-7] R. C. T. Slade, J. C. Southern and I. M. Thompson, *Journal of Materials Chemistry,* 1991, **1**, 563-568.

[4-8] M. H. Lee, C.-F. Cheng, V. Heine and J. Klinowski, *Chemical Physics Letters*, 1997, **265**, 673-676.

[4-9] R. H. Meinhold, R. C. T. Slade and R. H. Newman, *Applied Magnetic Resonance*, 1993, **4**, 121-140.

[4-10] F. R. Chen, S. Sheng, W. Zhang, X. Guo and J. J. Fripiat, *Journal of the Chemical Society, Faraday Transactions*, 1992, **88**, 887-890.

[4-11] K. J. D. MacKenzie, J. Temuujin and K. Okada, Thermochimica Acta, 1999, **327**, 103-108.

[4-12] C. Pecharroman, I. Sobrados, J. E. Iglesias, T. Gonzalez-Carreno and J. Sanz, *The Journal of Physical Chemistry B*, 1999, **103,** 6160-6170.

[4-13] S.D. Jackson, J.S.J.Hargreaves. *Metal oxide catalysis,* 2008, 1, Wiley-VCH.

[4-14] J. H. Kwak, J. Hu, D. Mei, C.-W. Yi, D. H. Kim, C. H. F. Peden, L. F. Allard and J. Szanyi, *Science*, 2009, **325,** 1670-1673.

[4-15] A. Düvel, E. Romanova, M. Sharifi, D. Freude, M. Wark, P. Heitjans and M. Wilkening, *The Journal of Physical Chemistry C*, 115, 22770-22780.

5 Conclusion

Anode properties of MgH_2 for the all solid state LIB are investigated. Moreover, anode properties of Nb_2O_5 doped MgH_2 and Al_2O_3 doped MgH_2 are investigated to clarify the role of additive metal oxide to MgH_2 by various types of experiments. The results are summarized as follows,

1. The insertion and extraction reactions of lithium ions from and into the pristine MgH_2 phase of the all solid state LIB were investigated. Upon the Li insertion, the entering of 3.1 mol g^{-1} Li ions into the cathode. Upon the Li extraction, 2.3 mol g^{-1} Li ions still remained in the cathode as LiH. The XRD profiles after the lithium insertion at x = 3.1 showed peaks corresponding to the lithium magnesium alloys and LiH phases. These results suggest that MgH_2 reacts with Li ions electrochemically, producing Mg and LiH even if the experiments were performed by the all solid state LIBs as follows,

$$MgH_2 + 2Li^+ + 2e^- \leftrightarrow Mg + 2LiH$$

Furthermore, Mg reacted with Li ions, producing hcp and bcc type lithium–magnesium alloys. The peak intensity corresponding to MgH_2 slightly increased for the x = 0.8sample, indicating that Li ion extraction did not completely proceed. On the other hand, the peaks corresponding to Mg and LiH were observed for the x = 0.8 sample, indicating that 74% of the entering Li ions remained in the cathode.

2. Coulombic efficiency of the first cycle was improved from 26% (pristine MgH_2) to 37% ($99MgH_2$-$1Nb_2O_5$) by adding Nb_2O_5. Moreover, coulombic efficiency increased from 37% to 56% with increasing Nb_2O_5 contents (Nb_2O_5 contents: 0 mol% to 5 mol%). The effect of the Nb_2O_5 additive on anode properties at high current or at low temperature was clearer than that at low current density or at high temperature. Coulombic efficiency of the first cycle was improved from 26% (pristine MgH_2) to 39% ($99MgH_2$-$1Al_2O_3$) by adding Al_2O_3. Moreover, coulombic efficiency increased from 39% to 52% with increasing Al_2O_3 contents (Al_2O_5 contents: 0 mol% to 25 mol%).

In the case of Nb_2O_5 doped MgH_2, the hydrogen desorption temperature decreases with increasing Nb_2O_5 contents, and coulombic efficiency increased with increasing Nb_2O_5 contents. Namely, coulombic efficiency was improved with decreasing hydrogen desorption temperature.

In the case of A_2O_3 doped MgH_2, the hydrogen desorption temperature did not decrease with increasing Al_2O_3 contents. On the other hand, coulombic efficiency was increased with increasing Al_2O_3 contents. Namely, coulombic efficiency was improved by Al_2O_3, but hydrogen desorption temperature did not depend on Al_2O_3 contents.

It is known that Al atom in γ-Al_2O_3 occupied octahedral coordination (AlO_6) and tetrahedral coordination (AlO_4). In the case of $75MgH_2$-$25Al_2O_3$, the distribution of AlO_6 was increased and the distribution of AlO_4 was decreased after Li insertion reaction. In addition, peak position of octahedral coordination shifts slightly to high magnetic field region and pentahedral coordination (AlO_5) is observed at around 33 ppm. This could act as a binding site for LiH. As a result, the path of hydrogen

diffusion between Mg phase and LiH phase is remained, leading to the increasing of coulombic efficiency.

As mentioned above, Nb_2O_5 acts to accelerate hydrogen ad/desortption reactions and Al_2O_3 acts to maintain the path of hydrogen diffusion. Namely, there exist two types of effect of metal oxide additives on anode properties of MgH_2. One is decreasing activation energy of hydrogen ab/desorption into/from Mg/MgH_2, which lead to high coulombic efficiency. The other is maintaining hydrogen diffusion path between Mg and LiH, which lead to high coulombic efficiency as well.

Thus “hydrogen” is the key and it is important how hydrogen is diffused between Mg and Li. In this thesis, it is clarified that anode properties of MgH_2 is improved by accelerating the hydrogen ab/desorption reactions and maintaining the hydrogen diffusion path in electrode.

公表論文

(1) Anode properties of magnesium hydride catalyzed with niobium oxide for an all solid-state lithium-ion battery
Suguru Ikeda, Takayuki Ichikawa, Koji Kawahito,
Kazuhiro Hirabayashi, Hiroki Miyaoka and Yoshitsugu Kojima
Chemical Communications, **49**, 7174-7176 (2013).

ChemComm

RSC Publishing

COMMUNICATION

View Article Online
View Journal | View Issue

Cite this: *Chem. Commun.*, 2013, **49**, 7174

Received 27th May 2013,
Accepted 26th June 2013

DOI: 10.1039/c3cc43987a

www.rsc.org/chemcomm

Anode properties of magnesium hydride catalyzed with niobium oxide for an all solid-state lithium-ion battery†

Suguru Ikeda,[a] Takayuki Ichikawa,*[ab] Koji Kawahito,[a] Kazuhiro Hirabayashi,[a] Hiroki Miyaoka[c] and Yoshitsugu Kojima[ab]

The anode properties of pristine MgH_2 and MgH_2 catalyzed with Nb_2O_5 have been investigated for an all solid-state lithium-ion battery. The catalytic effect stabilizes the plateau voltage as a result of kinetic improvement of the hydrogen transfer from the Mg phase to the Li phase.

Lithium ion batteries (LIBs) are key devices for energy storage to achieve a highly energy-efficient society in the future. LIBs with high energy-density have been used mainly for portable devices and electric vehicles in recent years. However, for the utilization of renewable energy sources such as solar, tidal, and wind power, because of the specific properties with fluctuation and maldistribution, highly functional secondary batteries should be developed to supply electricity on-demand originating from renewable energy sources. LIBs could be vital devices as candidates for functional batteries to utilize renewable energy efficiently in the future.[1,2] Recently, Oumellal *et al.* demonstrated the anode properties of MgH_2 for LIBs, experimentally indicating that MgH_2 has a large reversible capacity of 1480 mA h g^{-1} with an average voltage of 0.5 V (theoretical voltage is 0.560 V) *versus* Li^+/Li.[3,4] Actually, MgH_2 has potential as a LIB anode, showing 2038 mA h g^{-1} as the theoretical capacity by the following reaction,

$$MgH_2 + 2Li^+ + 2e^- \leftrightarrow Mg + 2LiH. \quad (1)$$

The group also reported that MgH_2 showed low polarization during the electrode conversion. Then, they considered that this polarization usually originates from poor mass transport kinetics and the H^- ions are expected to diffuse faster than the O^{2-} or F^- ions, therefore MgH_2 shows low polarization. In addition, they observed that the reaction of Li ion insertion–extraction produced nano-sized Mg and MgH_2. Furthermore, they confirmed the Li ion insertion reaction of other binary hydrides (TiH_2, NaH) and ternary hydrides ($LaNi_{4.25}Mn_{0.75}H_5$, $Mg_2NiH_{3.7}$) experimentally by XRD patterns, indicating the coexistence of LiH with another phase, being Ti, Na, $LaNi_{4.25}Mn_{0.75}$, or Mg_2Ni. On the other hand, MgH_2 is a promising hydrogen storage material, because magnesium has a high hydrogen storage capacity of 7.6 mass% and exists abundantly on the Earth. However, the slow kinetics and requirement of a high temperature, more than 300 °C, on the reaction of hydrogen ab/desorption have been barriers to the practical use of MgH_2 as a hydrogen storage material.[5,6] By adding a transition metal and metal oxide as a catalyst, the hydrogen sorption kinetics has been improved.[7–10] Barkhordarian *et al.* clarified that niobium oxide (Nb_2O_5) was the most effective catalyst among other metal oxides (such as Fe_3O_4, V_2O_5, Mn_2O_5, and so on) to improve the kinetics of the hydrogen ab/desorbing reaction.[11,12] Moreover, Hanada *et al.* reported that the Nb_2O_5-catalyzed MgH_2 was rehydrogenated even at room temperature.[13,14]

All solid-state LIBs are also candidates for future LIBs to overcome some safety issues. In order to improve charge–discharge properties, high performance solid electrolytes are required, which show high lithium ionic conductivity of at least 10^{-3} S cm^{-1}. Sulfide based solid electrolytes show high lithium ionic conductivity.[15–18] Li_2S–P_2S_5 glassy material is a sulfide based solid electrolyte, which can be obtained by the mechanical milling of Li_2S and P_2S_5.[19] This amorphous solid electrolyte has a high conductivity and wide electrochemical window. Actually, Li_2S–P_2S_5 is a precursor of glass ceramic electrolytes, and for example $Li_7P_3S_{11}$ was synthesized by a solid state reaction from $70Li_2S$–$30P_2S_5$ (mol%), showing that this solid electrolyte has a high lithium conductivity of 3.2×10^{-3} S cm^{-1} at room temperature.[20]

In this paper, we have focused on MgH_2 as an anode material for LIBs. Then, the anode properties of MgH_2 for an all solid-state LIB were investigated using the $80Li_2S$–$20P_2S_5$ solid electrolyte which was prepared by the mechanical milling method. In addition, the catalytic effect of Nb_2O_5 was attempted

[a] *Graduate School of Advanced Sciences of Matter, Hiroshima University, 1-3-1 Kagamiyama, Higashi-Hiroshima 739-8530, Japan*
[b] *Institute for Advanced Materials Research, Hiroshima University, 1-3-1 Kagamiyama, Higashi-Hiroshima 739-8530, Japan. E-mail: tichi@hiroshima-u.ac.jp; Fax: +81 82 424 5744; Tel: +81 82 424 5744*
[c] *Institute for Sustainable Science and Development, Hiroshima University, 1-3-1 Kagamiyama, Higashihi-Hiroshima 739-8530, Japan*

† Electronic supplementary information (ESI) available: Experimental details. See DOI: 10.1039/c3cc43987a

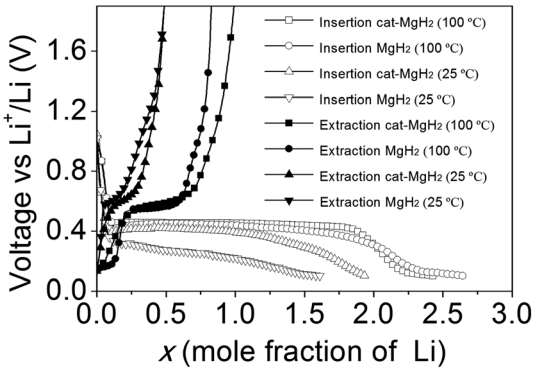

Fig. 1 VC curves corresponding to the Li ion insertion and extraction.

to be clarified during the insertion reaction of Li into the MgH_2 anode.

Fig. 1 shows the voltage and composition (VC) curves of pristine and catalyzed MgH_2 for an all solid-state LIB. The open and solid circles revealed, respectively, the Li ion insertion and extraction reactions of pristine MgH_2 ($MgH_2 + 2Li^+ + 2e^- \leftrightarrow Mg + 2LiH$) at a current density of 0.05 mA cm^{-2} at 100 °C. Upon the Li insertion, the voltage dropped suddenly in the range from $x = 0$ to $x = 0.1$, and showed a plateau feature with a gradual decrease from 0.45 V ($x = 0.1$) to 0.1 V ($x = 2.65$), which was consistent with the results reported by Oumellal *et al.*[3] In this Li insertion reaction, 2.65 mol g^{-1} lithium ions entered the cathode, forming LiH and a lithium–magnesium alloy. Upon the Li extraction, two plateaus were observed, and the lower and higher plateaus were located at 0.1 V and 0.56 V, respectively. After the voltage reached 2.3 V, 1.8 mol g^{-1} Li ions still remained in the cathode as LiH, indicating that 68% of the entering Li ions in the cathode could not be extracted. The VC curve of the Li ion insertion corresponding to the catalyzed MgH_2 by Nb_2O_5 (open square) shows a clear plateau in voltage located at 0.45 V between $x = 0.1$ and $x = 1.9$. After that, the VC curve gradually decreased to a voltage of 0.1 V in the range up to $x = 2.45$ with a current density of 0.05 mA cm^{-2} at 100 °C. It should be noted that the plateau features became more stable (clearer) when adding Nb_2O_5, than without Nb_2O_5. In other words, this stabilization of the plateau indicated that the Nb_2O_5 catalyst for the hydrogen desorption kinetics of MgH_2 also improved the kinetics of the electrochemical reaction to transfer a hydrogen atom from the Mg phase to the Li phase. Actually, in the case of pristine MgH_2, the voltage decreased by 24% in the range of $x = 0.4$ to $x = 1.9$, whereas, in the case of catalyzed MgH_2, the voltage only decreased by 12% in the corresponding range. Upon the lithium extraction of catalyzed MgH_2 (solid squares), the VC curve showed a plateau at 0.58 V, but the lower plateau located at 0.1 V, which was seen on the extraction reaction of the pristine MgH_2, was not observed. After the voltage reached 2.3 V, 1.4 mol g^{-1} Li ions still remained in the cathode as LiH, indicating that 58% of the entering Li ions in the cathode could not be extracted.

The VC curve of Li insertion reaction corresponding to the pristine/catalyzed MgH_2 (open inverted triangles/open triangles) at a current density of 0.005 mA cm^{-2} and at 25 °C showed that Li ions were inserted at room temperature. The voltage of the pristine MgH_2 (empty inverted triangles) suddenly dropped to 0.3 V at $x = 0.1$, and then gradually decreased to 0.1 V as a plateau-like feature upon Li insertion of 1.6 mol g^{-1} into the Mg cathode. On the other hand, the VC curve of the catalyzed MgH_2 showed a plateau located at 0.4 V in the range from $x = 0.1$ to $x = 1.0$, and after that, the VC curve gradually decreased to 0.1 V up to $x = 1.94$. The Li ion conductivity at 25 °C was lower than that at 100 °C, therefore, the current density at 25 °C needed to be smaller than that at 100 °C for the insertion reaction. In the case of pristine MgH_2, the voltage decreased by 66% in the range of $x = 0.1$ to $x = 1.5$, whereas, in the case of catalyzed MgH_2, the voltage decreased by 26% in the same range, which means that the catalyst, Nb_2O_5, can stabilize the plateau at 25 °C as well. Moreover, it is clear that the effect of stabilization of the plateau by Nb_2O_5 at 25 °C was more obvious than that at 100 °C. This indicates that the hydrogen transfer process from the Mg phase to Li phase is a rate-determined process at 25 °C. On the Li extraction reaction, although both the VC curves of the pristine and the catalyzed MgH_2 (solid inverted triangles/solid triangles) showed a plateau feature around 0.6 V and extracted 0.48 mol g^{-1} Li ions after the voltage reached 2.3 V, the plateau of the catalyzed MgH_2 had a larger capacity than that of the pristine MgH_2. These properties were consistent with the results at 100 °C.

Fig. 2 shows the XRD profiles of pristine MgH_2 before the lithium insertion ($x = 0.0$), after the lithium insertion ($x = 2.65$), and after the lithium extraction ($x = 0.85$). The peaks corresponding to MgH_2 were observed in the profile of $x = 0.0$, and they disappeared after the lithium insertion at $x = 2.65$. Lithium–magnesium alloys (Li_3Mg_{17} and Li_3Mg_7) and LiH phases were observed at $x = 2.65$. These results suggest that MgH_2 reacts with lithium ions electrochemically and transforms into LiH and Mg as the first step, then Mg reacts with lithium ions and transforms into a hcp-type lithium–magnesium alloy (Li_3Mg_{17}) as the second step, and afterwards reacts with lithium ions, transforming into a bcc-type lithium–magnesium alloy (Li_3Mg_7) as the third step.[21] The intensity of the peaks corresponding to MgH_2 increased slightly in the $x = 0.85$ sample, indicating that lithium ion extraction partially proceeded. In addition, although no peaks corresponding to Mg were recognized in the $x = 0.85$ profile, the plateau was seen at 0.1 V in the VC curve

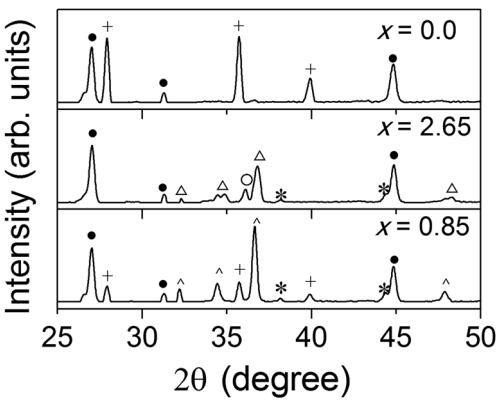

Fig. 2 XRD profile of pristine MgH_2 at 100 °C, 0.1 V, for $x = 0.0$ (MgH_2, before Li ion insertion), $x = 2.65$ (Mg + LiH, after Li ion insertion) and $x = 0.85$ (MgH_2, after Li ion extracted). ●: Solid electrolyte, +: MgH_2, △: Li_3Mg_{17}, *: LiH, ^: Mg, ○: Li_3Mg_7.

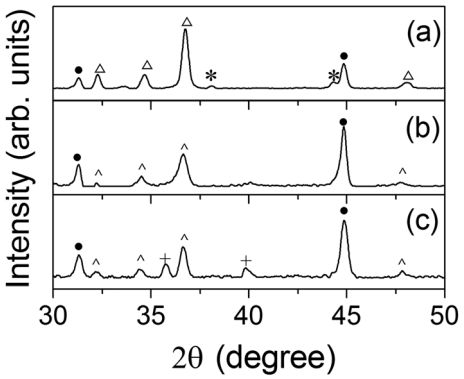

Fig. 3 XRD profiles of catalyzed MgH_2 at 100 °C, 0.1 V (a), catalyzed MgH_2 at 25 °C, 0.1 V (b) and pristine MgH_2 at 25 °C, 0.1 V (c) after Li ion insertion. ●: Solid electrolyte, +: MgH_2, △: Li_3Mg_{17}, *: LiH, ^: Mg.

for the lithium extraction of pristine MgH_2 at 100 °C (Fig. 1). The peaks corresponding to LiH were observed in the $x = 0.85$ profile, which is consistent with the fact that 68% of the entering lithium ions remained in the cathode electrode.

Fig. 3 shows the XRD profiles after lithium insertion of three samples, which were the catalyzed MgH_2 charged by a current density of 0.05 mA cm^{-2} at 100 °C (Fig. 3a) and 0.005 mA cm^{-2} at 25 °C (Fig. 3b), and the pristine MgH_2 charged by a current density of 0.005 mA cm^{-2} at 25 °C (Fig. 3c). The profile of sample (a) revealed that a hcp type lithium–magnesium alloy (Li_3Mg_{17}) and LiH were produced after the lithium insertion. Because the peaks corresponding to Mg were revealed in the profiles of both the catalyzed and pristine MgH_2 charged at 25 °C, the lithium ion insertion reaction into the MgH_2 phase proceeded at room temperature using the all solid-state electrolyte for LIB. The peaks corresponding to MgH_2 were observed only in the profile of pristine MgH_2 (Fig. 3c), indicating that MgH_2 remained in the cathode without reacting with lithium ions due to worse reaction kinetics.

In this work, the insertion and extraction reactions of lithium ions from and into the pristine MgH_2 phase of an all solid-state LIB were investigated. Upon Li insertion, the voltage showed a plateau located at 0.45 V and gradually decreased in the range up to $x = 2.65$ at 100 °C with the entering of 2.65 mol g^{-1} Li ions into the cathode. Upon Li extraction, two plateaus were observed, that is, the lower plateau was located at 0.1 V and the higher one was located at 0.56 V. After the voltage reached 2.3 V, 1.8 mol g^{-1} Li ions still remained in the cathode as LiH. The XRD profiles after the lithium insertion at $x = 2.65$ showed peaks corresponding to the lithium magnesium alloys and LiH phases. These results suggest that MgH_2 reacts with Li ions electrochemically, producing Mg and LiH. In addition, Mg reacted with Li ions, producing hcp and bcc type lithium–magnesium alloys. The peak intensity corresponding to MgH_2 slightly increased for the $x = 0.85$ sample, indicating that Li ion extraction did not completely proceed. On the other hand, the peaks corresponding to Mg and LiH were observed for the $x = 0.85$ sample, indicating that 68% of the entering Li ions remained in the cathode electrode.

The VC curve corresponding to MgH_2 catalyzed by Nb_2O_5 had a clear plateau voltage located at 0.45 V in the mole fraction range from $x = 0.1$ to $x = 1.9$ at 100 °C. The plateau was more stable than that of pristine MgH_2, indicating that Nb_2O_5 improved the kinetics of the electrochemical reaction and enabled transfer of hydrogen atoms from the Mg phase to the Li phase due to decreasing activation energy of H_2 ab/desorption of MgH_2.[12,13] The XRD profile of catalyzed MgH_2 corresponding to $x = 2.65$ reveals that lithium–magnesium alloys and LiH were produced after the lithium insertion.

Surprisingly, Li ions were inserted into both the pristine and catalyzed MgH_2 even at room temperature. The plateau of the catalyzed MgH_2 was more stable than that of the pristine MgH_2, indicating that Nb_2O_5 also stabilized the plateau at room temperature. Moreover, it is clear that the effect of stabilization of the plateau by Nb_2O_5 at room temperature was more obvious than at 100 °C.

The experimental investigation using an all solid-state electrolyte should provide more detailed information of the anode material before and after the electrochemical reactions compared with liquid-state electrolytes, because a special treatment prior to some analytical measurements is not necessary. As a next step, we will try to solve the low first discharge–charge efficiency and to clarify the mechanism of the worse cycle properties from a microscopic point of view.

This work was partially supported by the project ''Advanced Fundamental Research on Hydrogen Storage Materials'' of the New Energy and Industrial Technology Development Organization (NEDO). The authors gratefully acknowledge Mr Kazuhiro Hirabayashi and Mr Koji Kawahito for their help in this work.

Notes and references

1 J. M. Tarascon and M. Armand, *Nature*, 2001, **414**, 359–367.
2 M. Armand and J. M. Tarascon, *Nature*, 2008, **451**, 652–657.
3 Y. Oumellal, A. Rougier, G. A. Nazri, J. M. Tarascon and L. Aymard, *Nat. Mater.*, 2008, **7**, 916–921.
4 Y. Oumellal, A. Rougier, J. M. Tarascon and L. Aymard, *J. Power Sources*, 2009, **192**, 698–702.
5 B. Vigeholm, J. Kjoller and B. Larsen, *J. Less Common Met.*, 1980, **74**, 341–350.
6 B. Vigeholm, J. Kjoller, B. Larsen and A. S. Pedersen, *J. Less Common Met.*, 1983, **89**, 135–144.
7 G. Liang, J. Huot, S. Boily, A. Van Neste and R. Schulz, *J. Alloys Compd.*, 1999, **292**, 247–252.
8 A. Zaluska, L. Zaluski and J. O. Ström-Olsen, *J. Alloys Compd.*, 1999, **288**, 217–225.
9 W. Oelerich, T. Klassen and R. Bormann, *J. Alloys Compd.*, 2001, **315**, 237–242.
10 N. Hanada, T. Ichikawa and H. Fujii, *J. Phys. Chem. B*, 2005, **109**, 7188–7194.
11 G. Barkhordarian, T. Klassen and R. Bormann, *Scr. Mater.*, 2003, **49**, 213–217.
12 G. Barkhordarian, T. Klassen and R. Bormann, *J. Alloys Compd.*, 2004, **364**, 242–246.
13 N. Hanada, T. Ichikawa, S. Hino and H. Fujii, *J. Alloys Compd.*, 2006, **420**, 46–49.
14 N. Hanada, T. Ichikawa and H. Fujii, *J. Alloys Compd.*, 2007, **446–447**, 67–71.
15 J. H. Kennedy and Y. Yang, *J. Solid State Chem.*, 1987, **69**, 252–257.
16 S. Kondo, K. Takada and Y. Yamamura, *Solid State Ionics*, 1992, **53–56**, 1183–1186.
17 R. Kanno and M. Murayama, *J. Electrochem. Soc.*, 2001, **148**, A742–A746.
18 N. Kamaya, K. Homma, Y. Yamakawa, M. Hirayama, R. Kanno, M. Yonemura, T. Kamiyama, Y. Kato, S. Hama, K. Kawamoto and A. Mitsui, *Nat. Mater.*, 2011, **10**, 682–686.
19 A. Hayashi, S. Hama, H. Morimoto, M. Tatsumisago and T. Minami, *J. Am. Ceram. Soc.*, 2001, **84**, 477–479.
20 F. Mizuno, A. Hayashi, K. Tadanaga and M. Tatsumisago, *Solid State Ionics*, 2006, **177**, 2721–2725.
21 S. Brutti, G. Mulas, E. Piciollo, S. Panero and P. Reale, *J. Mater. Chem.*, 2012, **22**, 14531–14537.

